The Astrophysical Journal, 1011:217 (20pp), 2026 November 10 https://doi.org/10.3847/1538-4357/aeace4
© 2026. The Author(s). Published by the American Astronomical Society.
OPEN ACCESS

New Constraints on *r*-process Nucleosynthesis in Neutron Star Mergers from GW170817 Late-phase Spectra

Salma Rahmouni[1], Masaomi Tanaka[1,2], Daiji Kato[3,4], Gediminas Gaigalas[5], and Kenta Hotokezaka[6]
[1] Astronomical Institute, Tohoku University, Aoba, Sendai 980-8578, Japan; rahmouni.salma@astr.tohoku.ac.jp
[2] Division for the Establishment of Frontier Sciences, Organization for Advanced Studies, Tohoku University, Sendai 980-8577, Japan
[3] National Institute for Fusion Science, 322-6 Oroshi-cho, Toki 509-5292, Japan
[4] Interdisciplinary Graduate School of Engineering Sciences, Kyushu University, Kasuga, Fukuoka 816-8580, Japan
[5] Institute of Theoretical Physics and Astronomy, Vilnius University, Saulėtekio Avenue 3, LT-10257 Vilnius, Lithuania
[6] Research Center for the Early Universe (RESCEU), Graduate School of Science, The University of Tokyo, 7-3-1 Hongo, Bunkyo, Tokyo 113-0033, Japan
Received 2026 July 16; revised 2026 September 18; accepted 2026 September 25; published 2026 November 4

Abstract

The neutron star merger event GW170817 provided the first direct evidence of *r*-process nucleosynthesis. Observed spectra of its electromagnetic counterpart AT2017gfo exhibited several features that encode information on the nature and abundance of the synthesized *r*-process elements. In this study, we investigate the late nebular-phase spectral features of the kilonova AT2017gfo, which provide important probes of the elemental abundance of the ejecta. We construct an analytic spectral model that computes emission features produced by the radiative decay of collisionally excited ions through allowed and forbidden transitions. By comparing our model to AT2017gfo, we identify La III and Ce III as the main contributors to the emission features at 1.4 and 1.6 μm, respectively. We also confirm Te III as the dominant contributor to the 2.1 μm feature proposed in previous works. We infer mass fractions of $X(\mathrm{La}) \approx 0.025$–$0.05$, $X(\mathrm{Ce}) \approx 0.05$–$0.1$, and $X(\mathrm{Te}) \approx 0.04$–$0.08$, although the La and Ce abundance estimates remain tentative due to uncertainties in the radiation field. From the nondetections of Kr and Sb lines, we derive upper limits of $X(\mathrm{Kr}) \lesssim 0.03$ and $X(\mathrm{Sb}) \lesssim 0.003$. These results suggest that nucleosynthesis in the inner ejecta of GW170817 produced a suppressed first *r*-process peak and an enhanced abundance of heavier elements compared to the solar *r*-process pattern, with an estimated lanthanide fraction of $X_{\mathrm{LN}} \approx (3\text{–}6) \times 10^{-2}$. Our conclusions are consistent with the apparent universality of heavy *r*-process elements and the lanthanide fraction inferred from observations of *r*-enhanced metal-poor stars.

Unified Astronomy Thesaurus concepts: Atomic data (2216); Neutron stars (1108); Spectral line identification (2073)

1. Introduction

The coalescence of compact objects involving a neutron star has long been considered one of the primary sites for the nucleosynthesis of heavy elements through the rapid neutron capture process (*r*-process; e.g., J. M. Lattimer & D. N. Schramm 1974; E. Symbalisty & D. N. Schramm 1982; D. Eichler et al. 1989; C. Freiburghaus et al. 1999; S. Goriely et al. 2011; S. Wanajo et al. 2014). The decay of the freshly synthesized elements in such events powers an electromagnetic emission that can be observed in the infrared, optical, and ultraviolet wavelengths, known as kilonovae (L.-X. Li & B. Paczyński 1998; B. D. Metzger et al. 2010; L. F. Roberts et al. 2011).

The first direct observational evidence for *r*-process nucleosynthesis came in 2017 with the detection of gravitational waves (GW170817; B. P. Abbott et al. 2017a) from a binary neutron star merger (NSM), where follow-up observations detected an electromagnetic counterpart (AT2017gfo; B. P. Abbott et al. 2017b). The luminosity and color evolution of this event were consistent with theoretical expectations of kilonovae (e.g., I. Arcavi et al. 2017; E. Pian et al. 2017; S. J. Smartt et al. 2017; Y. Utsumi et al. 2017), which proved that heavy elements were synthesized in this event (e.g., D. Kasen et al. 2017; M. Shibata et al. 2017; M. Tanaka et al. 2017; K. Kawaguchi et al. 2018; S. Rosswog et al. 2018; A. Perego et al. 2019).

Constraining the elemental abundance synthesized in GW170817 is necessary to investigate whether NSMs can account for all *r*-process elements in the Universe. To achieve this goal, several studies have identified and investigated atomic features in the early-phase spectra of AT2017gfo. D. Watson et al. (2019) proposed Sr II as the main candidate for the 1 μm absorption feature, an identification that was subsequently confirmed by radiative-transfer simulations (N. Domoto et al. 2021; J. H. Gillanders et al. 2022). Recent findings suggest that this feature may be blended with He I when non–local thermodynamic equilibrium (non-LTE) populations are considered (A. Perego et al. 2022; Y. Tarumi et al. 2023; A. Sneppen et al. 2024; A. Arya et al. 2026; K. Chiba et al. 2026). The 0.7 μm absorption feature was attributed to Y II (A. Sneppen & D. Watson 2023, but see also Q. Pognan et al. 2023). Two additional prominent infrared absorption features, detected at 1.2 and 1.4 μm, were attributed to La III and Ce III, respectively (N. Domoto et al. 2022, 2023; M. Tanaka et al. 2023), although the 1.2 μm feature may also contain contributions from Gd III (S. Rahmouni et al. 2025). While the aforementioned studies have provided valuable abundance constraints (e.g., N. Domoto et al. 2021, 2022; J. H. Gillanders et al. 2022; A. Sneppen & D. Watson 2023), they mainly reflect the composition of the outer layer of the ejecta due to the optically thick conditions at the early phase.

Original content from this work may be used under the terms of the Creative Commons Attribution 4.0 licence. Any further distribution of this work must maintain attribution to the author(s) and the title of the work, journal citation and DOI.

While the early-phase spectra of AT2017gfo have been extensively studied, spectral features observed at the late phase remain more challenging to interpret. This difficulty arises from the increasing importance of nonthermal effects caused by high-energy particles produced during the decay of freshly synthesized elements. Identifying the late-phase features of kilonovae is particularly important because they provide a direct probe of the elemental abundance distribution synthesized during the merger due to the optically thin conditions of the ejecta. Several studies have investigated the late-phase evolution of the ejecta while accounting for non-LTE effects (e.g., K. Hotokezaka et al. 2021; Q. Pognan et al. 2022a, 2023, 2026; A. Jerkstrand et al. 2026). Using physical conditions characteristic of the late phase inferred from such simulations, K. Hotokezaka et al. (2023) proposed Te III as a likely candidate for the emission feature observed at 2.1 μm. This identification was subsequently confirmed by A. Jerkstrand et al. (2026) and Q. Pognan et al. (2026), although the latter argued that additional elements may also contribute to the feature. Two other prominent late-phase features are observed near 1.4 and 1.6 μm. For these features, J. H. Gillanders et al. (2024) proposed several possible candidates but did not reach definitive identifications. Recent non-LTE spectral simulations do not predict pronounced excess emission at these wavelengths (A. Jerkstrand et al. 2026; Q. Pognan et al. 2026), leaving the origin of these features largely unexplored.

One of the major challenges in the spectral investigation of kilonovae is the lack of complete and accurate atomic data. Solving for the ejecta evolution and modeling the late-phase spectra require transition probabilities and collisional rates for individual lines, as well as recombination and ionization rates for individual r-process elements. Although significant effort has focused on improving the atomic data required for non-LTE modeling (e.g., L. P. Mulholland et al. 2024a, 2024b, 2025, 2026b; S. Banerjee et al. 2025; D. J. Dougan et al. 2025; S. Bromley et al. 2026; L. P. Mulholland et al. 2026a), considerable uncertainties remain. This limitation is further compounded by the computational cost of treating large atomic datasets and solving for the populations of complex multilevel systems in non-LTE calculations. As a result, current late-phase spectral models typically include only a limited number of heavy elements and often rely on approximations for adopted atomic data (e.g., A. Jerkstrand et al. 2026; Q. Pognan et al. 2026). These challenges make it difficult to fully reproduce the observed spectra.

In this work, we construct an analytic spectral model capable of treating a much broader range of r-process elements than is currently feasible in non-LTE models, with the aim of reproducing and identifying the late-phase features observed in AT2017gfo. By inferring the relevant physical conditions directly from the observed spectra, we evaluate the expected luminosities of individual transitions using updated atomic data. The details of the model are introduced in Section 2. By comparing the model's predictions with the observed spectra, we identify La III, Ce III, and Te III as the main contributors to the emission features observed at 1.4, 1.6, and 2.1 μm, respectively. The relative importance of these species and the corresponding mass fraction constraints are discussed in Section 3. We examine the broader implications of our results in Section 4, and summarize our conclusions in Section 5.

2. Spectral Model

Our spectral model computes the luminosity emitted through the radiative decay of collisionally excited elements in an optically thin ejecta. In this section, we describe the basic equations underlying the model and the atomic data adopted to compute the emission lines of all species considered in this work.

2.1. Luminosity Evaluation

We assume that each transition can be treated independently by considering that it originates from a two-level energy system with energy separation ΔE. Under this approximation, transitions to and from other atomic levels are neglected. The balance between collisional excitation, collisional de-excitation, and radiative decay is therefore given by

$$n_e n_1 q_{12} = n_e n_2 q_{21} + n_2 \beta A_{21}, \tag{1}$$

where n_e is the electron density, n_k is the population of level k, and q_{12} is the collisional excitation rate coefficient, such that

$$q_{12} = \frac{8.629 \times 10^{-6}}{T_e^{1/2}} \frac{\Upsilon_{12}}{g_1} e^{-\Delta E/kT_e}. \tag{2}$$

Here T_e is the electron temperature, g_1 is the statistical weight of the lower level, and Υ_{12} is the velocity-averaged collision strength,

$$\Upsilon_{12} = \int_0^\infty \Omega_{12}(E) e^{-E/kT_e}\, d\left(\frac{E}{kT_e}\right). \tag{3}$$

E is the kinetic energy of the electron after the interaction, and Ω_{12} is the energy-specific collision strength, an atomic property related to the collisional excitation cross section of the transition in question. The collisional excitation and de-excitation rate coefficients satisfy the detailed balance relation

$$q_{12} = \frac{g_2}{g_1} q_{21} e^{-\Delta E/kT_e}. \tag{4}$$

The radiative rate from the upper level is given by $n_2 \beta A_{21}$, where A_{21} is the Einstein coefficient for spontaneous emission, while β accounts for the photon self-absorption and can be expressed as

$$\beta = \frac{1 - e^{-\tau}}{\tau}, \tag{5}$$

where τ is taken as the Sobolev optical depth in a homologously expanding ejecta

$$\tau = \frac{\pi e^2}{m_e c} n_1 t \lambda f. \tag{6}$$

Here, f and λ denote the oscillator strength and the wavelength of the transition, respectively. We note that the correction term due to stimulated emission is expected to be negligible under the conditions considered in this work.

The luminosity emitted per unit volume by a given transition is then obtained from the radiative decay rate

$$L = \Delta E \beta n_2 A_{21}. \tag{7}$$

It is useful to define the critical density of a transition as

$$n_{cr} = \frac{\beta A_{21}}{q_{21}}, \tag{8}$$

which corresponds to the density at which radiative decay and collisional de-excitation occur at comparable rates.

If $n_{\rm cr} < n_{\rm e}$, collisional de-excitation becomes important, and the upper level population can be approximated by a Boltzmann distribution $n_2 \approx n_i \frac{g_2}{Z_{\rm p}} e^{-E_2/kT_{\rm e}}$. The luminosity emitted per volume is therefore

$$L = \Delta E n_i \frac{g_2}{Z_{\rm p}(T_{\rm e})} e^{-E_2/kT_{\rm e}} \beta A_{21}, \tag{9}$$

where n_i is the number density of the ion, $Z_{\rm p}$ ($T_{\rm e}$) is its partition function, and E_k is the energy of level k.

Conversely, if $n_{\rm cr} > n_{\rm e}$, radiative decay dominates over collisional de-excitation, and we may assume $n_2 \beta A_{21} \approx n_2 n_1 q_{12}$. In our model, we consider only excitations occurring from the ground or from metastable levels. The population of the lower level can therefore be approximated by a Boltzmann distribution, and the luminosity emitted per volume is

$$L = \Delta E n_{\rm e} n_i \frac{g_1}{Z_{\rm p}(T_{\rm e})} e^{-E_1/kT_{\rm e}} q_{12}. \tag{10}$$

2.2. Atomic Data

2.2.1. Radiative Transitions

Due to their complex atomic structure, collisionally excited energy levels of heavy elements subsequently decay through both allowed and forbidden channels. Therefore, we include in our model allowed electric dipole (E1) and forbidden magnetic dipole (M1) and electric quadrupole (E2) transitions, selected using the method introduced by S. Rahmouni et al. (2025).

Energy-level data of each ion with atomic number $30 \leqslant Z \leqslant 90$ in our model are extracted from the National Institute of Standards and Technology Atomic Spectra Database (NIST ASD; A. Kramida et al. 2024). For elements with $91 \leqslant Z \leqslant 99$, we use the Selected Constants Energy Levels and Atomic Spectra of Actinides (SCASA; J. Blaise & J.-F. Wyart 1994) database. For Nd III ($Z = 60$), we adopt the energy levels from M. Ding et al. (2024) due to the completeness of their data. Extracted energy levels are constructed from radiative transitions measured using laboratory spectroscopic experiments and are sufficiently accurate for performing spectral identifications. For completeness, we include in our model all neutral, singly ionized, doubly ionized, and triply ionized species available in the aforementioned atomic databases.

Allowed and forbidden transitions of each element are selected based on the rigorous selection rules governing the change in parity and total angular momentum,[7] and the wavelength of each transition is calculated using the energy differences between the extracted energy levels. We restrict our analysis to transitions occurring below an energy threshold of 2 eV (S. Rahmouni et al. 2025), as higher energy levels are unlikely to be populated at the typical plasma conditions at the late phase even when population by non-LTE effects is taken into account (Q. Pognan et al. 2022b).

The wavelengths of the selected E1, M1, and E2 transitions for all elements are shown in Figure 1, while elements excluded due to the lack of atomic data are indicated by gray-shaded regions. Selected E1 transitions are mainly due to lanthanides ($Z = 57$–71) and actinides ($Z = 89$–103). This is a consequence of the complex atomic structure of such elements, which shows a strong overlap of the low-lying configuration manifolds involving *f*-, *d*-, and *s*-orbitals. These overlapping configurations provide many low-lying levels of different parity within the adopted excitation-energy range, allowing many E1 transitions to be selected. In contrast, selected forbidden transitions may arise from a wide range of elements, with a particularly large number of M1 and E2 transitions for lanthanides and actinides, as well as for transition-metal regions with $Z = 40$–45 and $Z = 72$–78. This result is due to the many low-lying energy levels associated with open *d*- and *s*-shell configurations for such species. Since these levels have essentially the same parity, E1 transitions between them are forbidden, and radiative decay mainly proceeds through M1 and E2 transitions.

It is also noteworthy that the number of selected transitions decreases with increasing ionization state. Electrons in higher charged ions experience a larger effective nuclear charge, which results in more tightly bound electrons and an overall increase in the atomic energy scale. Consequently, neutral and weakly ionized species tend to possess a larger number of low-lying excited states and therefore more transitions below our 2 eV threshold, whereas triply ionized species generally have fewer transitions satisfying this criterion.

2.2.2. Collisional and Radiative Rates

Computing the luminosity of individual transitions requires both collision strengths and Einstein *A*-coefficients. However, comprehensive experimental measurements of these quantities are not available for all elements and ionization states considered in this work. We therefore adopt a two-step approach: (1) First, we employ a set of physically motivated approximations to estimate the collisional and radiative rates of all transitions in order to perform a comprehensive search for candidate spectral features. (2) Second, for the transitions identified as potentially important, we compute more accurate collision strengths and Einstein coefficients using the atomic structure code HULLAC (A. Bar-Shalom et al. 2001; see Appendix B). In the following, we describe the approximations adopted in the first step of our analysis.

For E1 transitions, the collision strengths are estimated using the van Regemorter semi-empirical formula (H. van Regemorter 1962)

$$\Upsilon_{12;\rm E1} = 2.39 P(x) \left(\frac{\lambda}{1\ \mu\rm m} \right)^3 \left(\frac{g_1 A_{21}}{10^6\ \rm s^{-1}} \right), \tag{11}$$

where $x = \Delta E/kT$. This approximation assumes the incident electron can be described as a plane wave and treats the electron–ion interaction as a perturbation. The Gaunt factor $P(x)$ provides a semi-empirical correction that accounts for additional interaction channels between the electron and ion. $P(x)$ is integrated over a range of electron velocities and has values typically within 0.2–1.04, tabulated in H. van Regemorter (1962). For the radiative rates, we adopt the Einstein *A*-coefficient from the calibrated theoretical calculations of A. Flörs et al. (2025) for singly and doubly ionized lanthanides. For all other ions, we assume $g_1 A_{21} = 10^6\ \rm s^{-1}$, a

[7] The rigorous selection rules are: E1: (1) parity change (2) $\Delta J = 0, \pm 1$ (except $0 \leftrightarrow 0$), M1: (1) no parity change (2) $\Delta J = 0, \pm 1$ (except $0 \leftrightarrow 0$), E2: (1) no parity change (2) $\Delta J = 0, \pm 1, \pm 2$ (except $0 \leftrightarrow 0$, $1/2 \leftrightarrow 1/2$, $0 \leftrightarrow 1$).

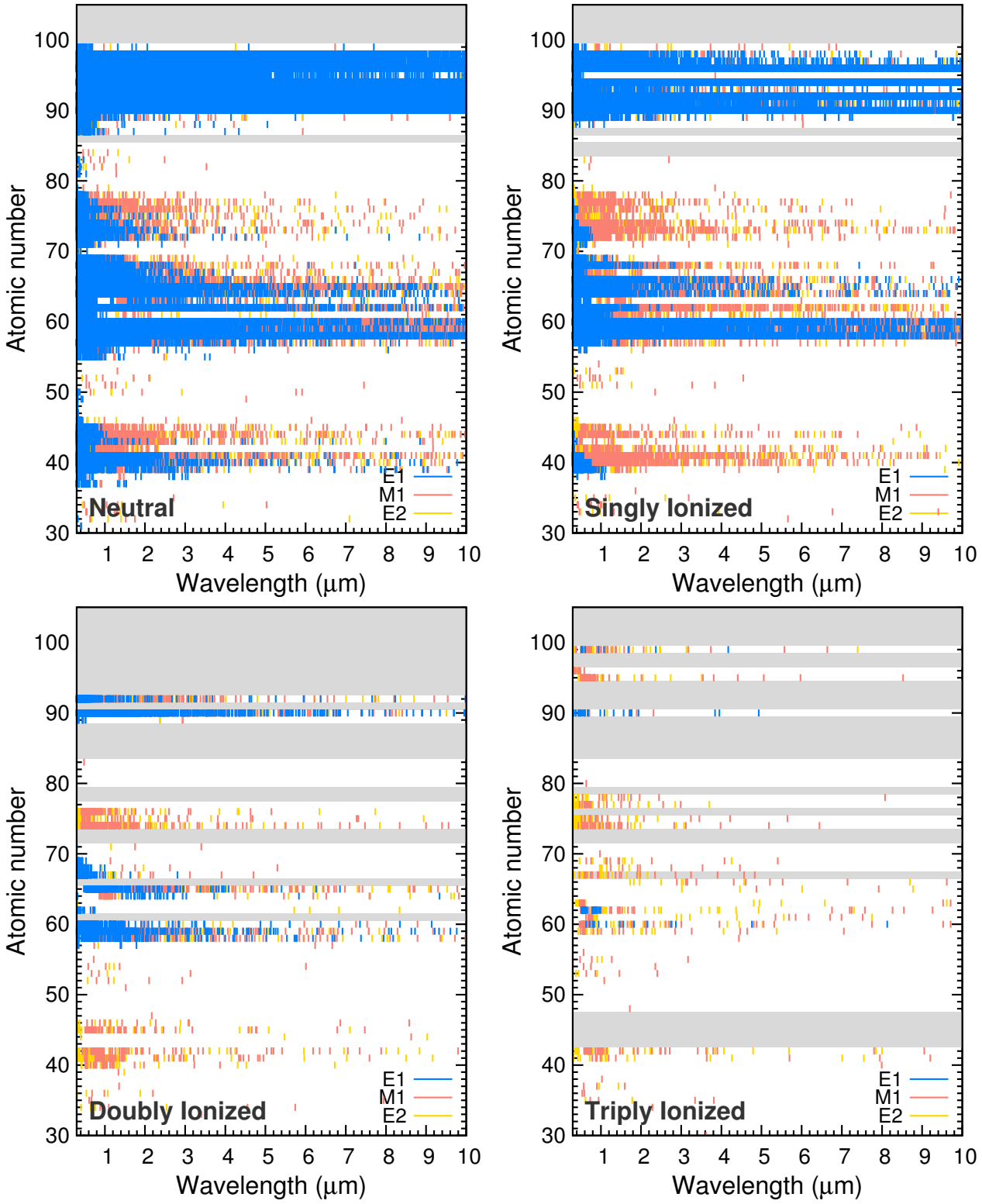


Figure 1. Selected transitions occurring below an energy threshold of 2 eV for neutral, singly, doubly, and triply ionized elements in the wavelength range of $\lambda = 0.3$–10 μm. E1, M1, and E2 transitions are highlighted in blue, red, and yellow, respectively. Elements excluded from our selection due to a lack of available energy levels are shown as gray-shaded areas.

value chosen to be broadly representative of strong transitions while lying toward the higher end of the distribution found in atomic databases (N. E. Piskunov et al. 1995; F. Kupka et al. 1999; T. Ryabchikova et al. 2015). For Th III ($Z = 90$), transition probabilities are available for a subset of transitions in Table 2 of N. Domoto et al. (2025). We adopt these tabulated values when available and use the representative value above for all other Th III transitions.

For M1 transitions, L. P. Mulholland et al. (2025) found that the collision strengths depend on the dominant open shell of

the ion. Their calculations yield $\Upsilon_{12;\mathrm{M1}} = 0.001$–$0.01$ for open d-shell systems and $\Upsilon_{12;\mathrm{M1}} = 0.1$–$1$ for open s-shell systems. Since the first step in our analysis is to identify all potentially relevant contributors to the observed spectra, we adopt a rather optimistic value of $\Upsilon_{12;\mathrm{M1}} = 1$ for all M1 transitions. The Einstein A-coefficient for fine-structure M1 transitions is calculated as follows (S. Pasternack 1940; G. H. Shortley 1940; J. N. Bahcall & R. A. Wolf 1968):

$$A_{21;\mathrm{M1}} = 82.3\left(\frac{\lambda}{1\ \mu\mathrm{m}}\right)^{-3} f(J, L, S)\ \mathrm{s}^{-1}, \tag{12}$$

where $f(J, L, S)$ is an algebraic factor depending on the orbital angular momentum L, spin S, and the total angular momentum J of the upper level, such as

$$f(J, L, S) = \frac{(J^2 - (L - S)^2)((L + S + 1)^2 - J^2)}{12J(2J + 1)} \tag{13}$$

if $J_2 = J_1 + 1$ and

$$f(J, L, S) = \frac{((J + 1)^2 - (L - S)^2)((L + S + 1)^2 - (J + 1)^2)}{12(J + 1)(2J + 1)} \tag{14}$$

if $J_2 = J_1 - 1$, where J_2 and J_1 are the total angular momentum of the upper and lower levels, respectively. For inter-configuration M1 transitions for which the above expressions are not applicable, we adopt a representative value of $A_{21;\mathrm{M1}} = 1\ \mathrm{s}^{-1}$, following previous works (K. Hotokezaka et al. 2021; G. Ricigliano et al. 2025).

For E2 transitions, previous calculations indicate collision strengths are of similar magnitude to M1 transitions, but generally have smaller Einstein coefficients (e.g., L. P. Mulholland et al. 2024b, 2026b). We therefore adopt $\Upsilon_{12;\mathrm{E2}} = 1$ and $A_{21;\mathrm{E2}} = 0.1\ \mathrm{s}^{-1}$ for all E2 transitions.

Since our objective in this first step is to identify candidate contributors, the adopted approximations are intended to provide order-of-magnitude estimates. More accurate atomic data are employed for the key transitions discussed in Section 3.

2.3. Resulting Spectrum

The model spectrum is obtained by summing the contributions from all selected E1, M1, and E2 transitions. As a fiducial case, we adopt an electron temperature of $T_\mathrm{e} = 2000$ K and an electron density of $n_\mathrm{e} = 10^7\ \mathrm{cm}^{-3}$ (K. Hotokezaka et al. 2023; J. H. Gillanders et al. 2024). Each transition is broadened using a Gaussian profile corresponding to an expansion velocity of $v = 0.07\,c$.

The abundance distributions adopted in our calculations are shown in Figure 2. The blue line shows the solar r-process abundance distribution (N. Prantzos et al. 2020), while the red line shows an abundance pattern with a suppressed first r-process peak and enhanced lanthanide fraction and third-peak abundances, which we refer to hereafter as the *heavy element-enhanced* abundance distribution. The heavy element-enhanced distribution was constructed by suppressing elements with $Z < 45$ by a factor of 10, and enhancing those with $Z > 56$ by a factor of 10, then renormalizing the mass fractions. These two distributions were selected as representative examples to explore how qualitatively different abundance patterns may affect the resulting spectra.

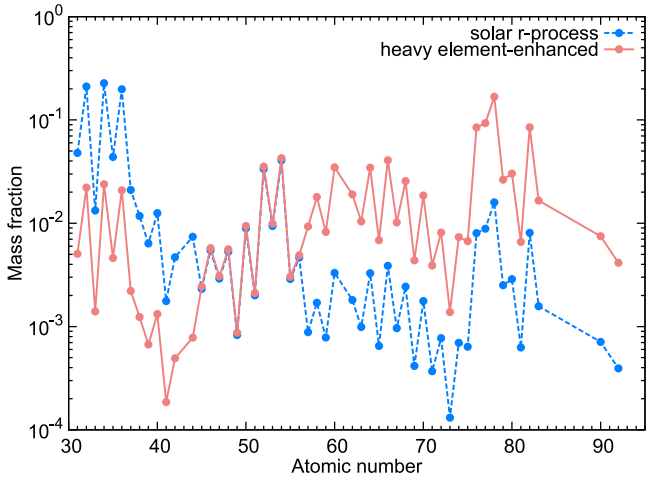


Figure 2. Abundance distributions used in this work. The blue line shows the solar r-process abundance pattern (N. Prantzos et al. 2020), while the red line shows the heavy element-enhanced pattern constructed by suppressing elements $Z < 45$ and enhancing elements $Z > 56$ each by a factor of 10, then renormalizing the mass fractions.

Previous non-LTE studies have shown that singly and doubly ionized species dominate at the epochs of interest (K. Hotokezaka et al. 2021; Q. Pognan et al. 2022a, 2026; A. Jerkstrand et al. 2026). Nevertheless, to avoid introducing assumptions about the ionization state when performing line identifications, we compute separate spectra for neutral, singly ionized, doubly ionized, and triply ionized species. As an illustrative example, Figure 3 shows the spectrum obtained for a doubly ionized composition. The left and right panels of the figure display the individual line contributions together with the total spectrum, where contributions from E1, M1, and E2 transitions are highlighted in blue, red, and yellow, respectively.

Figure 3 shows that both allowed and forbidden transitions can produce prominent emission features throughout the near- and mid-infrared wavelength ranges. The upper panels show the spectra assuming the solar r-process abundance pattern, where we find that the strongest features originate from fine-structure transitions of first-peak r-process elements such as Kr, Se, and As. In contrast, the spectra computed with the heavy element-enhanced abundance distribution (lower panels) show a few forbidden features, the strongest of which are produced by Te and W, both discussed in previous works (K. Hotokezaka et al. 2022, 2023). The model also predicts a few E1 features, most notably those of La III and Ce III in the near-infrared, together with stronger Th III features at mid-infrared wavelengths.

A notable characteristic of all our model spectra is the suppression of emissions at optical wavelengths ($\lambda < 1\ \mu$m). This behavior arises from their low collisional excitation rates at the typical temperature range in the kilonova ejecta at the late phase. Transitions at shorter wavelengths generally involve large excitation energies, and their collisional rates are exponentially suppressed as shown in Equation (2). Our results therefore indicate that the strongest collisionally excited emission features in the late-phase kilonovae are expected to emerge mainly at infrared wavelengths.

Overall, Figure 3 illustrates the potential of mid-infrared ($\lambda > 3\ \mu$m) observations for constraining the abundance distribution of the kilonova ejecta. An example is the kilonova candidate associated with GRB 230307A, which was observed

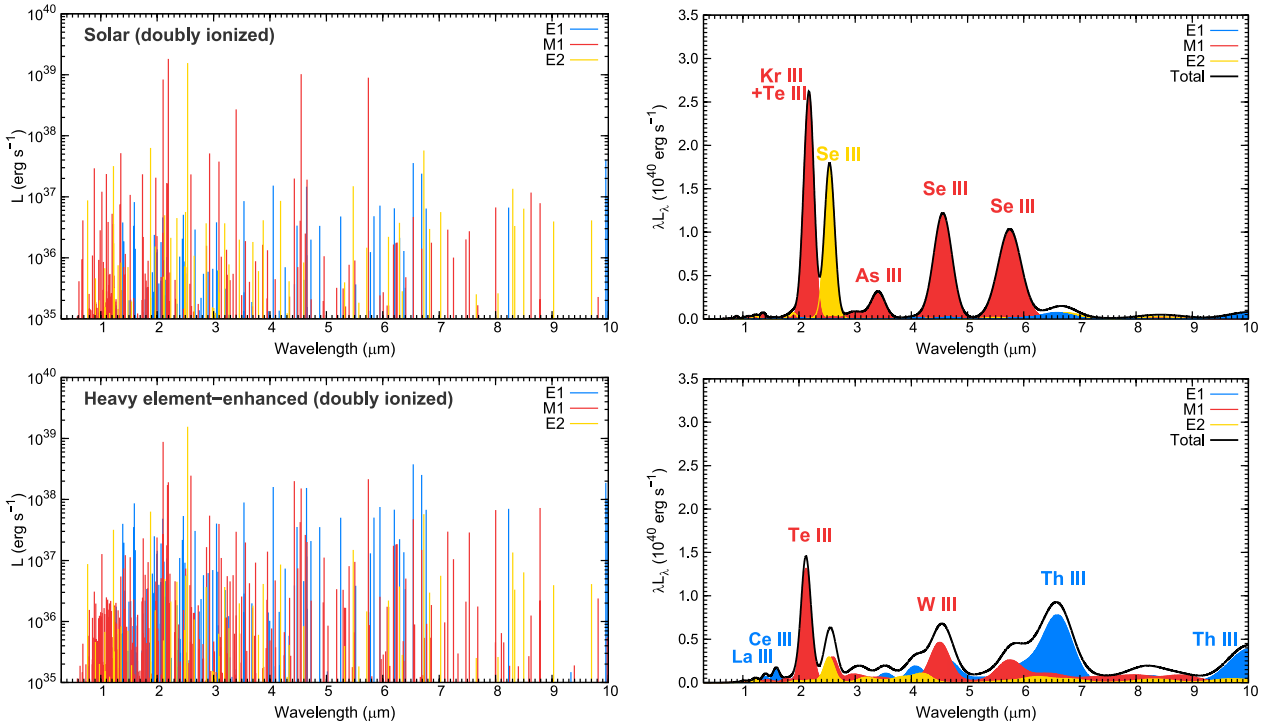


Figure 3. Left: calculated luminosity of individual transitions across the wavelength range of $\lambda = 0.3$–10 μm assuming an electron temperature $T_e = 2000$ K and $n_e = 10^7$ cm^{-3} as a fiducial model. The contributions from E1, M1, and E2 transitions are shown in red, blue, and yellow, respectively. A doubly ionized composition is assumed, and the solar *r*-process and heavy element-enhanced abundance patterns are assumed for the upper and lower panels, respectively. Right: the corresponding model spectra computed by assuming a Gaussian broadening of each line of $v = 0.07\,c$. The red, blue, and yellow regions show the contributions of E1, M1, and E2 transitions, and the total spectrum is shown in black. The strongest contributors for each produced feature are highlighted.

with JWST out to ∼5 μm at approximately 29 days after the gamma-ray burst detection (J. H. Gillanders et al. 2023; A. J. Levan et al. 2024). An emission feature consistent with both [Se III] 4.555 μm and [W III] 4.432 μm was reported (A. J. Levan et al. 2024; J. H. Gillanders & S. J. Smartt 2025; see also L. P. Mulholland et al. 2026a). However, the emergence of a continuum component, argued to be associated with dust (N. Domoto et al. 2026), complicated the identification of individual spectral features. These observations suggest that infrared spectra at earlier epochs may provide stronger constraints on the abundance distribution in future events.

3. AT2017gfo Spectral Analysis

3.1. Line Identification

The late-phase spectra of AT2017gfo show three main emission features centered near 1.4, 1.6, and 2.1 μm. The 1.6 and 2.1 μm features appear consistently and evolve throughout the late-phase spectrum observed with the Very Large Telescope (VLT; E. Pian et al. 2017; S. J. Smartt et al. 2017), while the 1.4 μm feature can only be observed in the spectrum taken with the Hubble Space Telescope (HST; N. R. Tanvir et al. 2017) due to the strong telluric absorption in the ground-based observations. We compare our model spectrum to the observed AT2017gfo to investigate whether we can reproduce the observed features. We use the observed spectrum at 9.4 days due to the availability of HST spectrum at the same epoch.

Figures 4 and 5 show the synthetic spectra assuming the solar *r*-process abundance and the heavy element-enhanced, respectively, with individual contributions of the most prominent transitions shown in colors. Each panel corresponds to a different ionization composition. The continuum is reproduced using a blackbody of temperature of $T = 1900$ K. We must note that a blackbody assumption may not hold at the late phase since the ejecta is expected to be at least partially optically thin at these epochs. In fact, the fit does not reproduce the observed continuum equally well at all wavelengths, and an emission excess can particularly be seen in the optical, as shown in Figures 4 and 5. As discussed in Section 2, we do not expect emission lines from collisional excitation in the optical wavelength range at the adopted temperature range, suggesting that this excess is unlikely to originate from blended line emission. Nevertheless, we consider that the blackbody model provides a reasonable fit to the continuum in the infrared where the features of interest are located, and we leave the discussion of its origin to future work.

As discussed in Section 2.3, the first *r*-process peak elements exhibit strong emission features when assuming the solar *r*-process abundance pattern. However, Figure 4 shows that none of the synthesized features provide a good match to the observed emission features of AT2017gfo. The results obtained with the heavy element-enhanced abundance distribution in Figure 5 show several features from lanthanides, along with contributions from species belonging to the first (Kr, Se), second (Te, Sn), and third (Ir, Os) *r*-process peaks. We find that our synthetic model assuming doubly ionized species gives a good match to the observed emission features, with the 1.4, 1.6, and 2.1 μm features attributed to La III, Ce III, and Te III, respectively. The mass fractions of each ion required to fully reproduce the features, as well as the effect of blending with other elements, are discussed in Section 3.3. We refer the reader to Appendix A for an in-depth discussion on

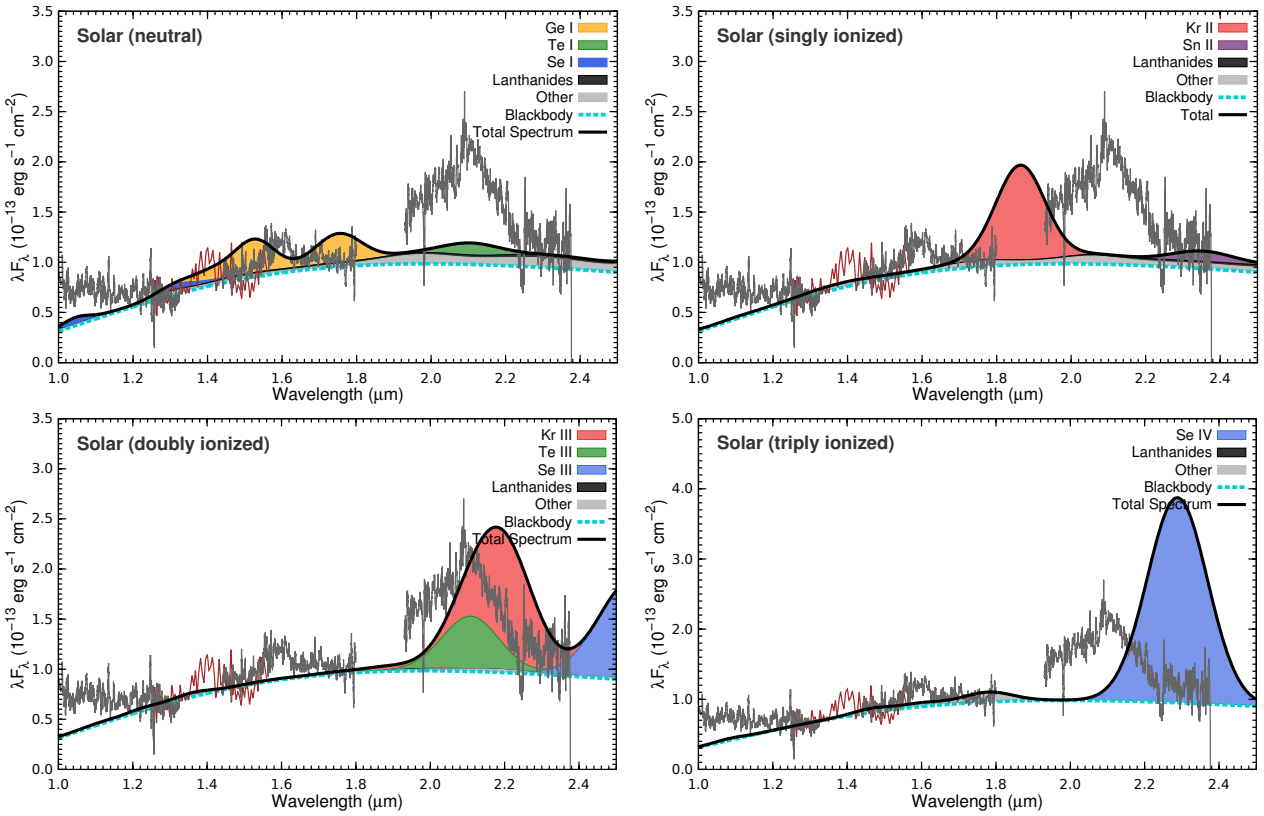


Figure 4. Comparison of our synthetic models calculated using the solar *r*-process abundance pattern to the 9.4 day spectrum of AT2017gfo observed with the VLT (black; E. Pian et al. 2017; S. J. Smartt et al. 2017) and the HST (brown; N. R. Tanvir et al. 2017). The continuum is reproduced assuming a blackbody of $T = 1900$ K. Each panel shows the results assuming a different ionization pattern, and the contribution of individual elements with prominent transitions is highlighted in different colors. The total spectrum in each panel is shown with a black line. We note that the synthetic spectra shown here are for the sake of comparison and are not intended to reproduce the observations.

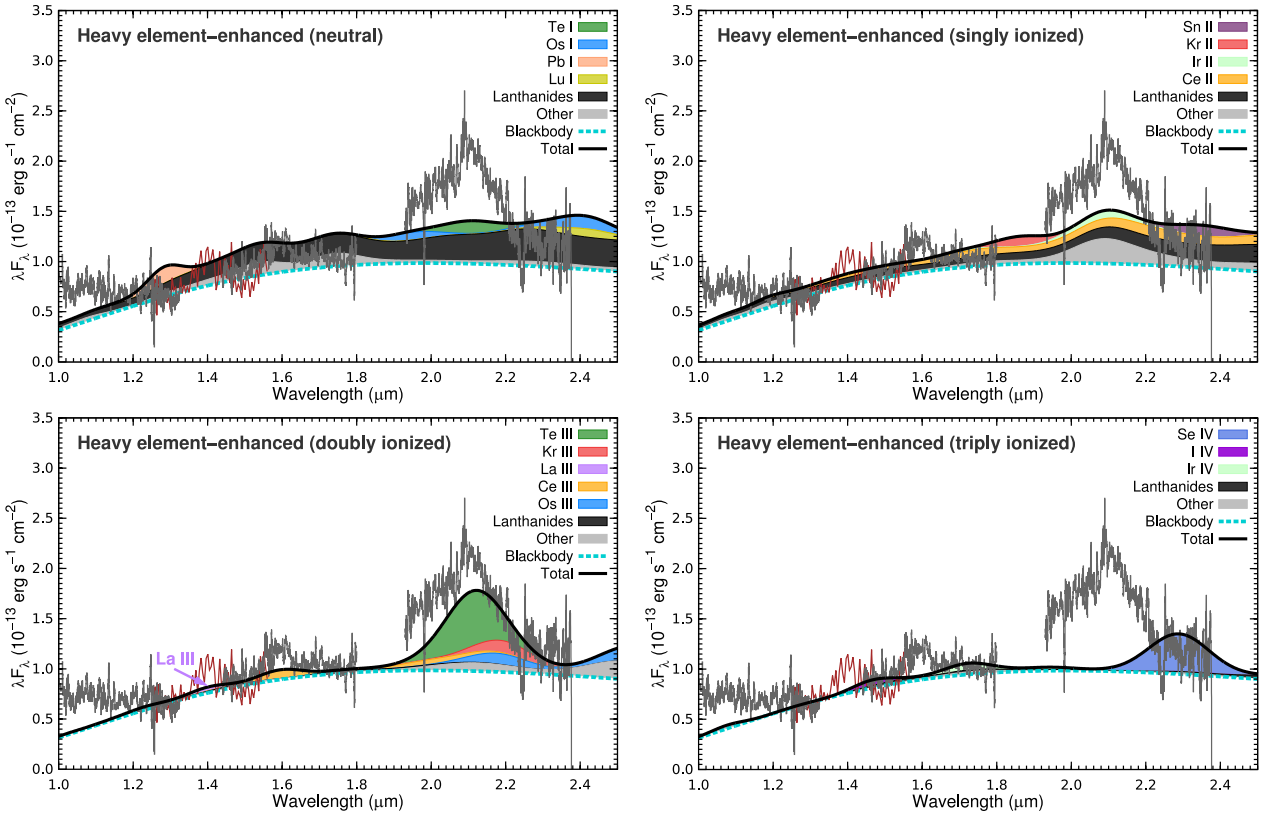


Figure 5. Same as Figure 4 but assuming the heavy element-enhanced distribution.

other possible candidates for each feature and their reasons for exclusion.

The importance of La and Ce among lanthanides stems from their relatively simple valence-electron structures. As a result, these elements exhibit several strong electric dipole transitions that can be observed in the near-infrared (N. Domoto et al. 2022). Indeed, these two elements have been proposed as the main candidates for two absorption features observed at 1.2–1.4 μm during the photospheric phase of AT2017gfo (N. Domoto et al. 2022). As the ejecta expands and becomes optically thin, the same transitions evolve from absorption to emission, making La III and Ce III strong candidates for the late-phase features identified here. This was also noted by J. H. Gillanders et al. (2024), who suggested La III and Ce III, among other candidates, as possible candidates for the 1.4 and 1.6 μm features.

The identification of Te III is motivated by a different mechanism. Te III possesses a strong fine-structure transition originating from its ground state, which was previously highlighted by K. Hotokezaka et al. (2023). In addition, Te belongs to the second *r*-process peak and is therefore expected to be synthesized in large quantities. The combination of a strong fine-structure transition and a potentially high abundance makes Te III a compelling explanation for the 2.1 μm feature.

3.2. Constraints on the Ionization Degree

Our search for candidate elements for each feature considers transitions from multiple ionization states (see also Appendix A). Nevertheless, the preferred identifications for all three observed features correspond to doubly ionized species. Previous works solving for the non-LTE evolution of kilonova ejecta generally predict that the relevant heavy elements are predominantly singly or doubly ionized at the epochs and velocities of interest (Q. Pognan et al. 2022a, 2026; A. Jerkstrand et al. 2026). Although a rigorous determination of the ionization composition requires a full non-LTE treatment with accurate atomic data, several observational arguments suggest that doubly ionized species dominate the formation of the observed emission features.

Ce II exhibits a dense forest of transitions extending from 1.4 μm up to and beyond 2.4 μm (upper right panel of Figure 5). If a large fraction of cerium were singly ionized, these Ce II lines would blend and obscure the isolated Ce III feature at 1.6 μm. The presence of a distinct and relatively narrow emission feature therefore suggests that Ce is predominantly doubly ionized during the late phase of AT2017gfo. Other lanthanides share similar ionization potentials as Ce, and they are all expected to occupy similar regions in the ejecta since they are synthesized under similar nucleosynthesis conditions. Therefore, other lanthanides, including La, most likely share the same dominant ionization state and are likewise mainly doubly ionized.

A similar argument can be given for Te III. Although we do not identify particularly strong transitions from other ionization states of Te, we find that Sn ($Z = 50$), an element neighboring Te ($Z = 52$) in the periodic table, has a strong feature at 2.3521 μm, produced in our model (see upper right panel of Figure 5). Moreover, our HULLAC calculations predict a collision strength more than three times higher than our original assumptions (Appendix B), meaning that this transition would produce a prominent feature if a large fraction of Sn were singly ionized. Because both Sn and Te are part of the second *r*-process peak, they are expected to be produced in broadly similar nucleosynthesis conditions. The absence of [Sn II] 2.3521 μm in the observed spectra suggests that the amount of Sn^+ is relatively small. This in turn favors a doubly ionized state of Te and other second *r*-process peak elements, since the two elements have comparable ionization potentials.

Motivated by these arguments, we hereafter adopt a doubly ionized composition of elements in our calculations. Nevertheless, we emphasize that robust constraints on the ionization degree of the ejecta ultimately require full non-LTE calculations that include the impact of all heavy elements.

3.3. Abundance Estimations from Detected Lines

3.3.1. La III (Z = 57)

La III is our best candidate for the 1.4 μm emission feature as it has two strong transitions at 1.3898 and 1.4100 μm. Both lines are E1 transitions with high transition probabilities, and critical densities satisfying $n_{\rm cr} > n_{\rm e}$. Therefore, their total luminosities are computed in the low-density limit described by Equation (10), yielding

$$L_{\rm La\,III} = \Delta E_{1.38}\, n_{\rm e} \frac{N_{\rm La\,III}}{Z_{p;\,\rm La\,III}} \frac{8.6\times10^{-4}}{\sqrt{T_{\rm e}}} \Upsilon_{1.38}\, e^{-E_{2;1.38}/k_{\rm B}T_{\rm e}} + \Delta E_{1.41}\, n_{\rm e} \frac{N_{\rm La\,III}}{Z_{p;\,\rm La\,III}} \frac{8.6\times10^{-4}}{\sqrt{T_{\rm e}}} \Upsilon_{1.41}\, e^{-E_{2;1.41}/k_{\rm B}T_{\rm e}},$$

where the subscripts 1.38 and 1.41 refer to La III at 1.3898 and 1.4100 μm respectively, and $E_{2;1.38}$ and $E_{2;1.41}$ indicate the upper levels of each of the two transitions. $N_{\rm La\ III}$ is the number of La^{2+} ions and $Z_{p;\rm La\ III}$ is the partition function. For the collision strengths $\Upsilon_{1.38}$ and $\Upsilon_{1.41}$, we used the results of our calculations using the atomic structure code HULLAC in Appendix B.

To reproduce the observed emission feature at each observed epoch, the electron density is parameterized as $n_{\rm e} = 10^7 (t/9.5\,\text{days})^{-3}\,\text{cm}^{-3}$, following previous works (K. Hotokezaka et al. 2023). The electron temperature, on the other hand, is assumed to be the best-fit blackbody temperature of the observed continuum, namely $T = 2400$, 2100, 1900, and 1700 K for the spectra observed at 7.4, 8.4, 9.4, and 10.4 days, respectively.

The left panel of Figure 6 compares the synthetic La III with the observations for different La mass fractions. We adopt a line broadening of $v = 0.05\,c$, which gives the best match to the observed line profile. Assuming that La is predominantly doubly ionized, the mass fraction is computed as $X_{\rm La} = N_{\rm La} A_{\rm La} m_{\rm u}/M_{\rm ej}$, where $A_{\rm La}$ is the La mass number, $m_{\rm u}$ is the atomic mass unit, and the ejecta mass is taken as $M_{\rm ej} = 0.05\,M_\odot$ (K. Hotokezaka & E. Nakar 2020).

The 1.4 μm feature is observed at a single epoch at 9.4 days after the merger with HST (N. R. Tanvir et al. 2017). To isolate the emission feature, we subtract a continuum obtained from a blackbody fit with $T = 1900$ K. Comparing the synthetic spectra with observations, we find that a mass fraction of $X(\text{La}) \approx X(\text{La III}) \approx 0.05$ provides the best match to the observed 1.4 μm feature. This value exceeds the lanthanum mass fraction expected from a solar *r*-process abundance distribution by more than 2 orders of magnitude (Figure 2).

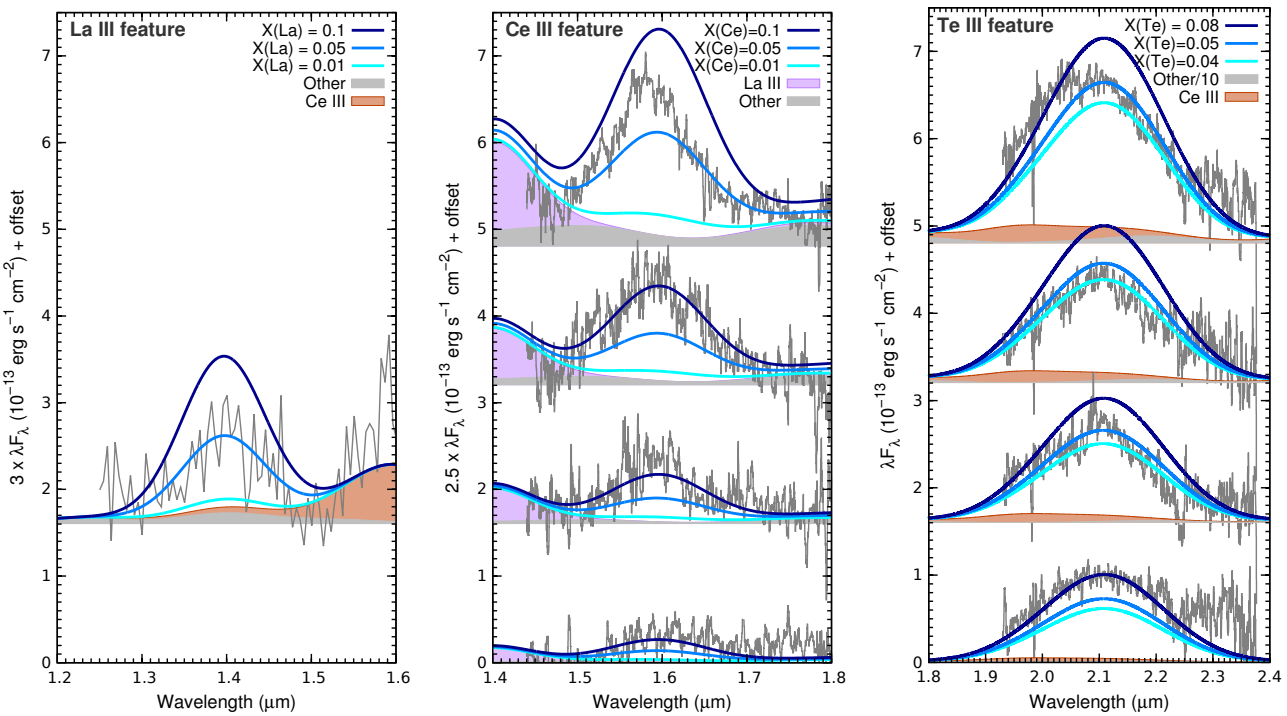


Figure 6. Comparison of our synthetic model to the observed features of AT2017gfo. The continua have been removed by assuming a blackbody of temperatures $T = 2400$, 2100, 1900, and 1700 K for the observations at 7.4, 8.4, 9.4, and 10.4 days, respectively. The synthetic spectra are computed assuming electron temperatures equal to the blackbody temperature and an electron density of $n_e = 10^7 (t/9.5\ \mathrm{days})^{-3}\ \mathrm{cm}^{-3}$. Left: comparison with the 1.4 μm feature in the HST spectrum at 9.4 days after the merger. Models with different La mass fractions are shown in different shades of blue with line broadening of $v = 0.05\,c$. The contribution from Ce III is shown in orange, while the combined contribution from all other elements is shown in gray. The flux is boosted by a factor of 3 for better visualization. Center: comparison with the 1.6 μm feature in the VLT spectra at 7.4, 8.4, 9.4, and 10.4 days after the merger (top to bottom). Models with different Ce mass fractions are shown in shades of blue with line broadening of $v = 0.05\,c$. The contribution from La III is shown in purple, and that from all other elements is shown in gray. The flux is boosted by a factor of 2.5 for better visualization. Right: comparison with the 2.1 μm feature in the VLT spectra. Models with different Te mass fractions are shown in shades of blue with line broadening of $v = 0.07\,c$. The contribution from Ce III is highlighted in orange. The combined contribution of other elements is shown in gray and has been suppressed by a factor of 10 (see the text).

3.3.2. Ce III (Z = 58)

Ce III is our best candidate for the 1.6 μm feature as it has three lines at wavelengths 1.5961, 1.5851, and 1.6133 μm. All three transitions have critical densities satisfying $n_{cr} > n_e$, and Ce III contribution can therefore be computed as

$$L_{\mathrm{Ce\,III}} = \Delta E_{1.59}\, n_e \frac{N_{\mathrm{Ce\,III}}}{Z_{p;\mathrm{Ce\,III}}} \frac{8.6\times10^{-4}}{\sqrt{T_e}} \Upsilon_{1.59}\, e^{-E_{2;1.59}/k_B T_e} + \Delta E_{1.58}\, n_e \frac{N_{\mathrm{Ce\,III}}}{Z_{p;\mathrm{Ce\,III}}} \frac{8.6\times10^{-4}}{\sqrt{T_e}} \Upsilon_{1.58}\, e^{-E_{2;1.58}/k_B T_e} + \Delta E_{1.61}\, n_e \frac{N_{\mathrm{Ce\,III}}}{Z_{p;\mathrm{Ce\,III}}} \frac{8.6\times10^{-4}}{\sqrt{T_e}} \Upsilon_{1.61}\, e^{-E_{2;1.61}/k_B T_e},$$

where the subscripts 1.59, 1.58, and 1.61 refer to Ce III at 1.5961, 1.5851, and 1.6133 μm, respectively. The energy-averaged collision strengths are taken from our HULLAC calculations (Appendix B).

The middle panel of Figure 6 shows the comparison of Ce III contribution to the observed 1.6 μm feature for different Ce mass fractions. The emission is isolated by subtracting a blackbody continuum of temperatures of $T = 2400$, 2100, 1900, and 1700 K for the observations at 7.4, 8.4, 9.4, and 10.4 days, respectively. Similarly to the 1.4 μm feature, a velocity broadening of $v = 0.05\,c$ provides the best match to the observed line profile. This suggests that elements responsible for both 1.4 and 1.6 μm features originate from ejecta regions with comparable velocity distributions, further supporting our identifications.

We find that a cerium mass fraction in the range of X(Ce) $\approx$ X(Ce III) $\approx$ 0.05–0.1 best reproduces the observed 1.6 μm feature. The variation in the preferred value between epochs may reflect changes in the ionization degree, departures from the assumed electron density, or uncertainties in the continuum subtraction. Nevertheless, the temporal evolution of the feature is broadly consistent with the gradual weakening predicted by the model as the ejecta cools and expands. At 9.4 days, the observed feature is best reproduced with X(Ce) = 0.1. Combined with the previously derived La abundance, we find a mass ratio between La and Ce of X(La)/X(Ce) $\approx$ 0.5, consistent with the value expected from a solar r-process abundance pattern, $(X(\mathrm{La})/X(\mathrm{Ce}))_\odot = 0.52$. We also find that Ce III feature is slightly affected by an emission line on its blue side, highlighted in gray in the middle panel of Figure 6. This feature is attributed to Sb III and is further discussed in Section 3.4.

3.3.3. Te III (Z = 52)

We identify [Te III] 2.1048 μm as the main contributor to the 2.1 μm feature, consistent with previous studies (K. Hotokezaka et al. 2023). For our estimates, we adopt the atomic data computed for this line by L. P. Mulholland et al. (2024b). Their atomic structure calculations are performed with the R-matrix method, which captures resonance interactions in the

cross sections. This gives a collision strength of $\Upsilon_{\mathrm{Te\ III}} \approx 3.5$ for $T_e = 2000$ K, a factor of a few higher compared to our HULLAC calculations (Appendix B).

The [Te III] 2.1048 μm transition satisfies $n_{cr} < n_e$ under the conditions relevant to AT2017gfo, its luminosity is therefore evaluated as

$$L_{\mathrm{Te\ III}} = \Delta E_{2.10} N_{\mathrm{Te\ III}} \frac{g_{2;2.10}}{Z_{p;\mathrm{Te\ III}}} e^{-\Delta E_{2;2.10}/k_B T_e} \beta A_{2.1},$$

where $g_{2;2.1}$ and $E_{2;2.1}$ are the statistical weight and energy of the upper level of [Te III] 2.1048 μm. The Einstein coefficient $A_{2.1}$ is also taken from L. P. Mulholland et al. (2024b).

The right-hand panel of Figure 6 compares the synthetic spectra with the observed 2.1 μm feature for different tellurium abundances. We find that a velocity broadening of 0.07 c provides the best match to the observed line profile. The Te III feature in our model is blended with other lines, notably those of Kr III, Os III, and Ce III (see bottom left panel of Figure 5). [Kr III] 2.1985 μm and [Os III] 2.1841 μm are both redward of the observed feature. The effect of the Kr III line is further discussed in Section 3.4. The [Os III] 2.1841 μm line is an inter-configuration M1 line that does not follow *LS*-coupling rules, and its contribution may be expected to be weaker than predicted by our fiducial model. Since we cannot provide updated atomic data for Os III due to its complex atomic structure (Appendix B), we leave further discussion of possible constraints on Os abundance to future work.

Although weak blending with other elements may be expected, Te III remains the main contributor to the 2.1 μm feature, as shown in the bottom left panel of Figure 5. Therefore, to minimize the dependence of our Te abundance estimate on assumptions regarding the abundances and atomic data of neighboring species, we reduce their contribution relative to the fiducial heavy element-enhanced abundance distribution. We highlight that the presence of Kr III and Os III in the spectra causes a spectral profile that is redshifted compared to observations, and reducing their abundance does not largely affect our estimates of X(Te) (see Section 3.4 for a discussion on the effect of Kr III). In contrast, Ce III is retained in the calculation because its abundance is independently constrained by the 1.6 μm feature. Also, collision strengths for the Ce III lines from our HULLAC calculations are available, providing a more physically motivated estimate than the approximations adopted initially. The strongest Ce III transitions contributing in this wavelength range occur at wavelengths of 1.9146, 1.9503, 1.9975, 2.0691, and 2.0987 μm.

We find that Te mass fractions in the range of X(Te) $\approx X$(Te III) $\approx$ 0.04–0.08 reproduce the observed feature across the available epochs. The variation in the required mass fraction may be due to changes in the ionization state or uncertainties in the subtracted continuum level. Our inferred abundance is somewhat larger than, but consistent with, the value obtained by K. Hotokezaka et al. (2023), who found $X(\mathrm{Te}^{2+}) \sim 0.02$. This difference is due to the different atomic data adopted in the two studies. Notably, the observed spectra show that the temporal evolution of the luminosity of the 2.1 μm feature is much weaker than that of the 1.6 μm feature. This behavior is consistent with our model, as the Te III emission does not depend on the electron density of the ejecta as long as $n_{cr} < n_e$ is satisfied, while Ce III emission declines rapidly since $L_{\mathrm{Ce\ III}} \propto n_e$.

Overall, the synthetic spectra provide a good match to the observed 2.1 μm feature at most epochs. The main exception occurs at 7.4 days, where the observed feature is blueshifted by approximately 0.03 μm compared to later observations. Similar behavior was previously noted by J. H. Gillanders et al. (2024), who suggested that this change in the line shape may result from the blending of the Te III emission line with an additional emission feature at $\sim$2.06 μm. Although Ce III in our model contributes several transitions blueward of the Te III feature, its abundance is already constrained by the 1.6 μm emission and does not appear sufficient to explain the observed evolution. More recently, K. Chiba et al. (2026) proposed that He I 2.059 μm line emission produced by non-LTE level populations may contribute to the observed feature. Investigating such effects requires a self-consistent treatment of non-LTE populations and is therefore beyond the scope of this work.

3.4. Upper Limits from Nondetected Lines

3.4.1. Kr II/Kr III (Z = 36)

Our model, assuming the solar *r*-process abundance pattern, predicts several prominent Kr emission lines that are not observed in the spectra of AT2017gfo (upper right and bottom left panels of Figure 4). The absence of these features can therefore be used to place upper limits on the Kr abundance in the ejecta. The nondetection of Kr was also previously discussed by K. Hotokezaka et al. (2023) and A. Jerkstrand et al. (2026).

Non-LTE calculations of A. Jerkstrand et al. (2026) show that Kr is expected to be predominantly singly ionized at the velocity and timescale of interest. This behavior differs from that of other elements discussed in this work, mainly because the ionization potential of Kr^+ is 24.3 eV, relatively high compared to 11.0 and 18.6 eV for Ce^+ and Te^+, respectively. Nevertheless, given the uncertainties in the ionization composition of the ejecta, we consider both singly and doubly ionized Kr when deriving abundance constraints. The transition probabilities and collisional cross sections are taken from our HULLAC calculations (Appendix B), while we use the R-matrix calculation results for the collision strength of [Kr III] 2.1986 μm ($\Upsilon_{\mathrm{Kr\ III}} \approx 3.8$; T. Schoning 1997).

The left panel of Figure 7 shows the case of a purely singly ionized Kr ((Kr^+, Kr^{2+}) = (1, 0)). Although the peak of [Kr II] 1.8622 μm falls within a region strongly affected by telluric absorption, its broad wings extend into neighboring wavelengths and become inconsistent with the observations for Kr mass fractions exceeding X(Kr) $\sim$ 0.03.

The middle panel of Figure 7 shows the case of (Kr^+, Kr^{2+}) = (0, 1). Here, we adopt half of the best-fit Te abundance, X(Te)/2, in order to investigate whether [Kr III] 2.1986 μm could be considered as an additional contributor to the observed 2.1 μm feature. We find that increasing the Kr abundance produces a noticeable redward shift of the synthetic feature relative to the observations. This allows an upper limit of approximately $X(\mathrm{Kr}) \lesssim 0.02$.

Given the uncertainty in the Kr ionization state, we adopt the more conservative limit, $X(\mathrm{Kr}) \lesssim 0.03$, as our final abundance constraint.

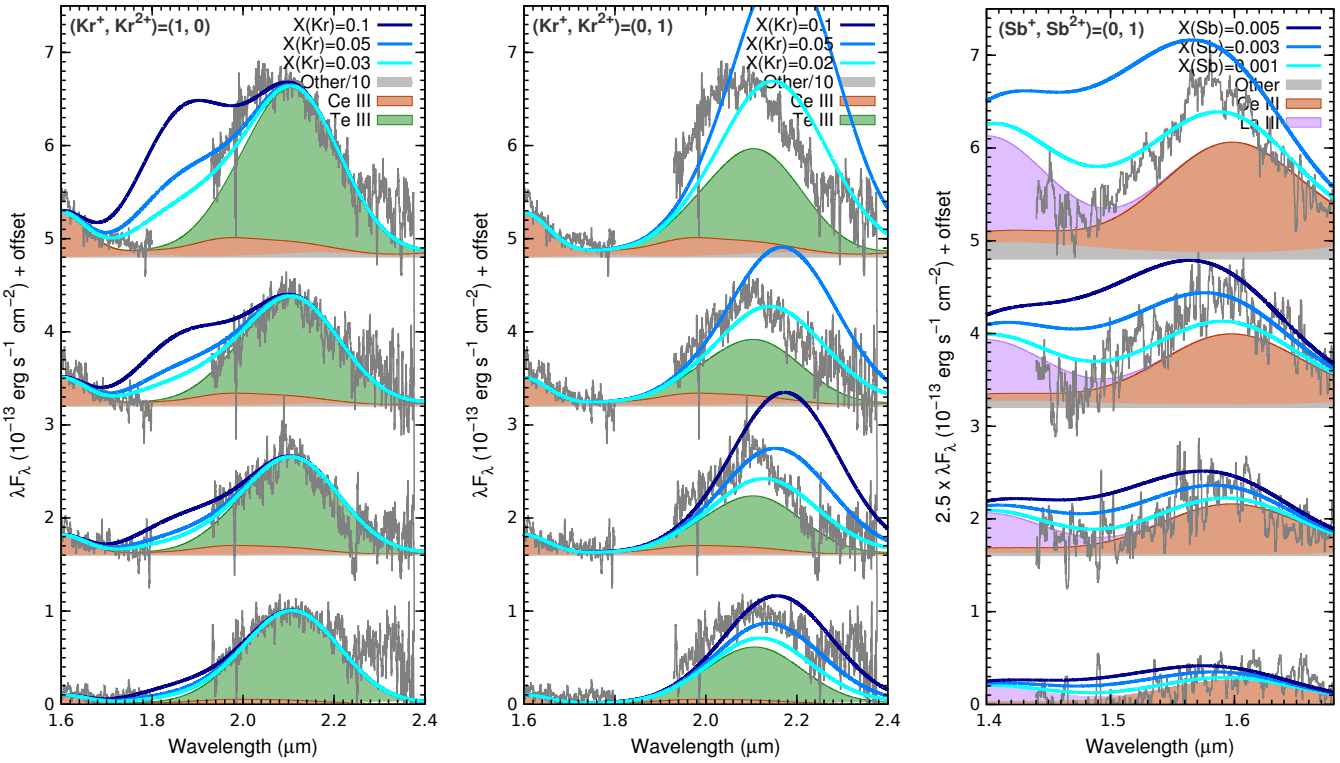


Figure 7. Same as Figure 6 but showing the effect of varying the abundances of Kr and Sb. Left: comparison of the synthetic spectra with the observed 2.1 μm feature of AT2017gfo, assuming different Kr mass fractions with (Kr^+, Kr^{2+}) = (1, 0) and line broadening of $v = 0.07\,c$. The contribution of Te is shown in green, while the contribution of other elements is suppressed by a factor of 10 and is shown in gray. Center: same as the left panel, but assuming (Kr^+, Kr^{2+}) = (0, 1). Here, half of the best-fit Te abundance (X(Te)/2) is assumed to investigate whether [Kr III] 2.1986 μm could be considered an additional contributor to the 2.1 μm feature. Right: comparison of the synthetic spectra with the observed 1.6 μm feature of AT2017gfo, assuming different Sb mass fractions with (Sb^+, Sb^{2+}) = (0, 1) and line broadening of $v = 0.07\,c$. The contribution from Ce is shown in orange, while the combined contribution of other elements is shown in gray.

3.4.2. Sb III (Z = 51)

Sb III possesses a strong fine-structure line with a wavelength of 1.5207 μm, located blueward of the Ce III feature. Because no corresponding emission feature is observed in AT2017gfo, the nondetection of this line can be used to constrain the abundance of Sb.

To derive an upper limit, we compare our synthetic spectra with observations, as shown in the right panel of Figure 7, while varying the Sb abundance. Since Sb belongs to the second r-process peak and is expected to share a similar ionization degree with Te, we assume that Sb is predominantly doubly ionized. A velocity broadening of $v = 0.07\,c$ is adopted, and the Ce and La abundances are fixed to the best-fit value derived in Section 3.3.

Increasing the Sb abundance produces a broad emission feature that blends with Ce III and La III, shifting the synthetic spectrum away from the observed profile. We therefore find that the mass fraction of Sb should satisfy $X(\mathrm{Sb}) \lesssim 0.001$ at 7.4 days, and $X(\mathrm{Sb}) \lesssim 0.003$ at 8.4 days and later epochs. Using the Te abundance derived at 8.4 days in Section 3.3, $X(\mathrm{Sb}) \lesssim 0.003$ gives $X(\mathrm{Sb})/X(\mathrm{Te}) \lesssim 0.075$, consistent with the solar r-process mass ratio $(X(\mathrm{Sb})/X(\mathrm{Te}))_\odot = 0.06$. It is noteworthy that our derived upper limit for Sb III at 7.4 days would give $X(\mathrm{Sb})/X(\mathrm{Te}) \lesssim 0.025$ assuming $X(\mathrm{Te}) = 0.04$, which falls below the solar r-process ratio. However, as discussed in Section 3.3, the modeling of the 2.1 μm feature at 7.4 days is subject to significant uncertainties because the observed line profile is not well reproduced by our Te III model. We therefore regard the later-epoch constraint as more robust.

Overall, the absence of detectable Sb III emission indicates that Sb is not significantly enhanced relative to Te and remains consistent with the abundance ratios expected for a solar-like second r-process peak, with a mass fraction upper limit of $X(\mathrm{Sb}) \lesssim 0.003$.

4. Discussion

4.1. Overall Picture

Using our analytical spectral model, we were able to give robust identifications to all three emission features observed in the late-phase spectrum of AT2017gfo, where we find La III, Ce III, and Te III to be the main candidates for the 1.4, 1.6, and 2.1 μm features, respectively. The corresponding mass fractions are $X(\mathrm{Te}) \approx 0.04$–$0.08$, $X(\mathrm{La}) \approx 0.05$, and $X(\mathrm{Ce}) \approx 0.05$–$0.1$. From the nondetection of Kr and Sb lines, we also infer mass fraction upper limits of $X(\mathrm{Kr}) \lesssim 0.03$ and $X(\mathrm{Sb}) \lesssim 0.003$. Figure 8 shows the comparison of our model computed with the derived best-fit mass fractions to the observed AT2017gfo spectrum. We use the observed spectra at 9.4 days due to the available HST spectrum at the same epoch.

The mass fractions and upper limits derived in this work are summarized in Figure 9. Since the mass fraction of La is estimated by a single epoch ($X(\mathrm{La}) \approx 0.05$), we derive the range of X(La) by assuming a constant mass ratio of La to Ce throughout all epochs. Therefore, based on the mass ratio X

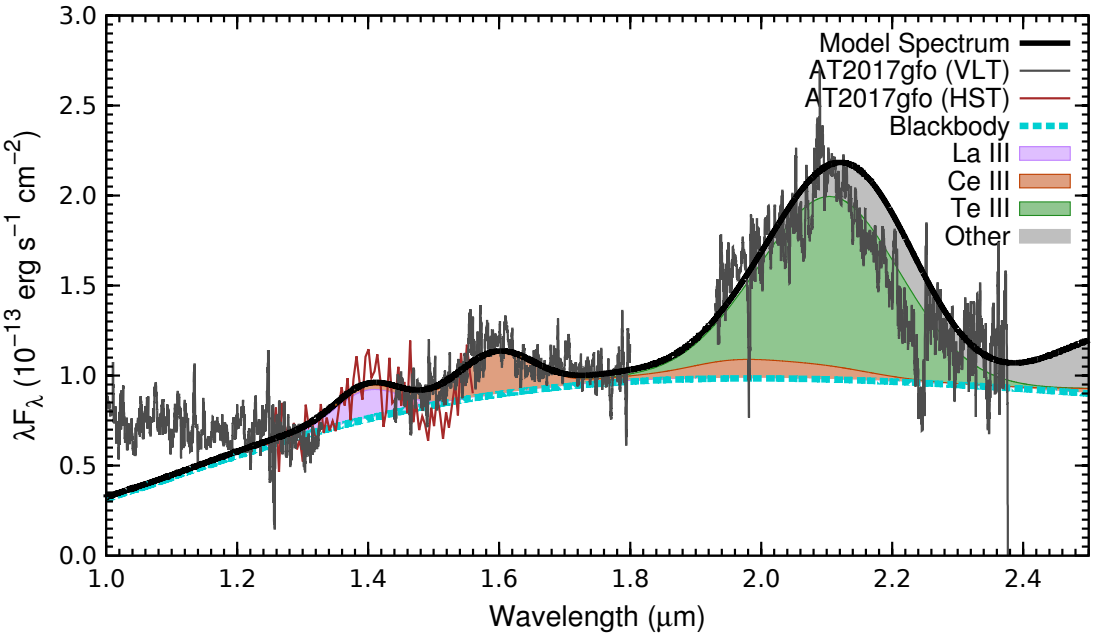


Figure 8. Comparison of our best-fit synthetic spectrum to the 9.4 day spectrum of AT2017gfo. The continuum is reproduced assuming a blackbody of $T = 1900$ K. The contributions of La III, Ce III, and Te III are computed with our best-fit mass fractions and are shown in purple, orange, and green, respectively. The combined contribution of all other elements with a doubly ionized state and the heavy element-enhanced abundance distribution is shown in gray.

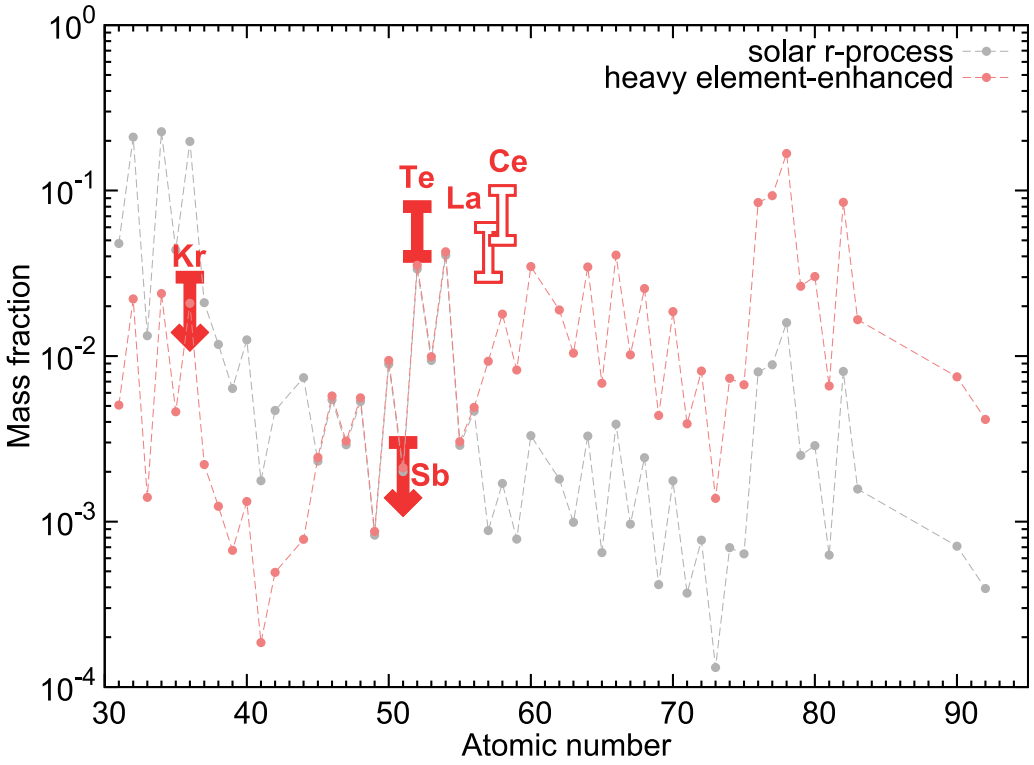


Figure 9. Summary of the abundance constraints inferred in this work. The constraints on La and Ce are tentative due to uncertainties of the radiation field and are shown as open symbols. The solar *r*-process and heavy element-enhanced abundance distribution patterns are shown in gray and red, respectively. We note that the error bars do not represent the uncertainties but rather the range of mass fractions inferred from our analysis (see Section 4.3).

(La)/X(Ce) ≈ 0.05 inferred from the 9.4 day observations, we find an estimated mass fraction range of X(La) ≈ 0.025–0.05.

Figure 9 shows that our constraints favor an abundance pattern characterized by a suppressed first *r*-process peak and enhanced production of heavy *r*-process elements. The low Kr abundance provides direct evidence against a solar-like first peak. This was previously suggested by K. Hotokezaka et al. (2023) and A. Jerkstrand et al. (2026). The detections of lanthanide species, on the other hand, require larger heavy-element abundances than expected from the solar pattern.

We highlight that the derived mass fractions of La and Ce may be uncertain, and we show them as open bars in Figure 9. Unlike Te III, which is observed through a forbidden transition, the La III and Ce III features arise from strong E1 transitions

that may remain sensitive to the radiation field. If part of the late-time continuum originates from an optically thick inner region, radiative excitation may still affect these transitions. In that case, P Cygni profiles may form even at the late phase. The absence of obvious absorptions blueward of the emission peaks suggests that such effects are not dominant. However, this conclusion is difficult to establish because the relevant wavelength regions are affected by telluric absorption, and because the continuum level is uncertain. To illustrate the sensitivity of these transitions to optically thick conditions, we consider an outer region of density $\rho = 10^{-17}\,\mathrm{g\,cm^{-3}}$ and temperature $T = 2000\,\mathrm{K}$ at $t = 10$ days. Using Equation (6), we find that the Sobolev optical depth of the strongest La III and Ce III lines reaches $\tau \sim 1$ for abundances as low as $X = 10^{-3}$, comparable to expectations from the solar *r*-process pattern. Nevertheless, such estimates are subject to uncertainties in the radiation field and the density of the possible line-forming region, and providing further abundance constraints is challenging. It is noteworthy, however, that the Gaussian-like shape of the forbidden line [Te III] suggests that the inner part of the ejecta is optically thin enough to emit collisionally excited forbidden transitions. This in turn supports collisional excitation as the main origin for Ce III and La III features.

This is an interesting physical situation unique to lanthanides (and actinides) that stems from the low-lying energy levels of Ce III and La III. This causes their strong E1 lines to slowly shift through time from radiative excitation by the radiation field to collisional excitation by free electrons. Quantifying when this shift occurs requires full understanding of the continuum and ejecta properties of the merger. We leave such discussion of the continuum to future work, and we propose our La and Ce mass fraction estimates as tentative.

4.2. Implications

Our work finds that the inner ejecta of GW170817 had a nucleosynthesis pattern with a suppressed first *r*-process peak, and enhanced heavy-element production relative to the solar *r*-process abundance distribution. Such an abundance pattern is consistent with expectations for the nucleosynthesis site responsible for heavy *r*-process element enrichment observed in *r*-enhanced metal-poor stars. It has long been recognized that the abundance pattern of heavy elements ($Z > 56$) in these stars closely follows the solar *r*-process pattern, suggesting a common nucleosynthesis origin, while lighter elements ($31 < Z < 50$) show a much larger star-to-star scatter, and do not show the same degree of universality (e.g., C. Sneden et al. 2003; I. U. Roederer et al. 2018, 2022). Our results therefore support a scenario in which NSMs are the dominant production site of the second *r*-process peak elements and beyond, while an additional astrophysical source may be required to explain the observed solar abundance of first-peak *r*-process elements.

A useful quantity for characterizing heavy-element production is the *lanthanide fraction*, defined as the total mass fraction of synthesized lanthanides. By analyzing the spectra of a sample of *r*-enhanced metal-poor stars, A. P. Ji et al. (2019) measured the lanthanide fraction and found a typical $X_{\rm LN} \approx 3 \times 10^{-2}$. They argued that their estimates are higher compared to the lanthanide fraction in GW170817, inferred from kilonova light-curve modeling, which gives $X_{\rm LN} = 2 \times 10^{-3} - 2 \times 10^{-2}$ (e.g., R. Chornock et al. 2017; C. D. Kilpatrick et al. 2017; M. Tanaka et al. 2017). However, A. Kitamura et al. (2025) recently cautioned against using the red and blue components of kilonovae to infer ejecta parameters due to the reprocessing of light from different components. This would therefore introduce uncertainties in the lanthanide fraction derived from light-curve modeling alone. J. H. Gillanders et al. (2026) recently modeled the observed early-phase spectra of AT2017gfo using updated atomic data from A. Flörs et al. (2025), and found that a lanthanide fraction of $X_{\rm LN} \approx 2.5 \times 10^{-3}$ gives the best match to observations. Similarly, N. Domoto et al. (2022) inferred cerium mass fractions of 10^{-5}–10^{-3} from radiative-transfer simulations of the early photospheric spectra, from which they derived $X_{\rm LN} \approx$ (2–200) $\times 10^{-4}$. However, due to the optically thick conditions at early-phase, such estimates are only representative of the outer ejecta layer.

Estimating the lanthanide fraction from our late-phase analysis is challenging because only a limited number of elements can currently be identified. Nevertheless, under the assumption that the relative abundances of heavy *r*-process elements follow the solar *r*-process abundance distribution, we extrapolate the abundance of lanthanides using the solar *r*-process pattern with our Te abundance estimate, where we find $X_{\rm LN} \approx (3\text{–}6) \times 10^{-2}$. We choose not to use the La and Ce abundances for this estimate because their inferred mass fractions may be affected by uncertainties associated with the radiation field, as discussed in Section 4.1. Interestingly, our inferred lanthanide fraction is consistent with the characteristic lanthanide fraction measured in *r*-enhanced metal-poor stars, $X_{\rm LN} \approx 3 \times 10^{-2}$ (A. P. Ji et al. 2019). This agreement further supports the idea that NSMs are the primary source of the lanthanides observed in these stellar populations.

The apparent discrepancy between our inferred lanthanide fraction and previous estimates based on early-phase spectra (N. Domoto et al. 2022; J. H. Gillanders et al. 2022, 2026) may suggest different abundance patterns in different layers of the ejecta. During the photospheric phase, the ejecta is optically thick, and the observed absorption features mainly probe the outermost ejecta within our line of sight. In the case of GW170817, observations indicate that the event was viewed at an angle close to the polar region (K. P. Mooley et al. 2018; G. Ghirlanda et al. 2019). Numerical simulations suggest that the polar ejecta are characterized by relatively high electron fractions and consequently lower lanthanide abundances compared to the equatorial ejecta (e.g., S. Fujibayashi et al. 2023). Abundance estimates derived from the photospheric phase may reflect the composition of the lanthanide-poor outer polar ejecta. In contrast, the late-time spectra analyzed in this work originate from the optically thin phase, where emission from a much larger fraction of the ejecta volume contributes to the observed spectrum. Consequently, our abundance estimates may better represent the overall nucleosynthesis yields of the event.

Finally, we revisit the question of whether NSMs can account for all of the *r*-process elements observed in the Milky Way. Assuming that the mean *r*-process in the Galaxy follows the solar *r*-process abundance pattern, with a total Galactic baryonic mass of $\sim 6 \times 10^{10}\,M_{\odot}$ (P. J. McMillan 2011), then the total mass of *r*-process elements in the Milky Way is $M_{r,A>69} \sim 23{,}000\,M_{\odot}$. Our main findings suggest that GW170817 mainly synthesized elements of the second *r*-process peak and beyond ($A > 115$; $Z > 49$). Therefore, if the nucleosynthesis in GW170817 is representative of NSMs, then such events would be responsible for producing

$M_{r,A>115} \sim 4000\,M_\odot$ of heavy r-process elements over the history of the Milky Way. The rate of NSMs needed to explain this observed amount of Galactic heavy r-process can be estimated such that (K. Hotokezaka et al. 2018; S. Rosswog et al. 2018)

$$R \sim 8\ \mathrm{Myr}^{-1}\left(\frac{M_{r,A>115}}{4000\,M_\odot}\right)\left(\frac{m_r}{0.05M_\odot}\right)^{-1}\left(\frac{t_{\mathrm{MW}}}{10\ \mathrm{Gyr}}\right)^{-1}, \quad (15)$$

where m_r is the ejecta mass per merger event, and is taken as $0.05\,M_\odot$ as was inferred for GW170817 (K. Hotokezaka & E. Nakar 2020).

The inferred rate is consistent with estimates from gravitational-wave observations, including 0.76–25 Myr^{-1} (A. G. Abac et al. 2026) and the more conservative estimate of 0.28–30 Myr^{-1} reported by M. Fishbach et al. (2026), inferred assuming a number density of Milky Way–like galaxies of $\approx$0.01 Mpc^{-3}. Our estimate assumes a constant star formation history for the Milky Way, and may further decrease by a factor of a few if the star formation burst expected during the early evolution of the Galaxy is taken into account (M. Fishbach et al. 2026). Although uncertainties remain, our results indicate that, if GW170817 is representative of NSMs, then a low inferred rate of these events can still explain the Galactic inventory of heavy r-process elements.

4.3. Caveats

Our work provides robust identification of all observed late-phase features of AT2017gfo, from which we derive constraints on the ejecta abundance distribution of key elements. In this section, we discuss the principal limitations of our analysis.

Our results depend strongly on the adopted atomic data. We use the HULLAC atomic structure code to provide the radiative and collisional rates necessary for our model. However, HULLAC calculations are restricted by the limited configuration space chosen to reduce the computational cost, as well as uncertainties regarding the choice of adequate configuration sets. Therefore, the La III and Ce III collision strengths may be subject to uncertainties associated with the calculated inter-configuration energies and wave functions, which may affect the inferred Ce and La mass fraction. For fine-structure forbidden lines, the effective collision strength may instead be underestimated because our HULLAC calculations do not capture resonance contributions to the cross sections. To mitigate this effect, R-matrix results of previous works are used (T. Schoning 1997; L. P. Mulholland et al. 2024b) when available. Nevertheless, we emphasize that theoretical calculations are generally subject to systematic uncertainties when treating heavy, multi-electron elements, and experimental measurements remain necessary.

In addition to uncertainties in atomic data, our treatment of the emission features adopts a two-level approximation for each transition. In reality, the populations of energy levels are coupled through radiative and collisional processes involving several levels, and cascades from higher-lying states may contribute to the population of the emitting levels (e.g., Q. Pognan et al. 2026). The treatment of such effects is challenging, particularly for complex r-process elements. Further theoretical atomic calculations and laboratory measurements of atomic data, together with spectral models incorporating multilevel treatment of heavy elements, are necessary to improve the abundance estimates presented in this work.

Our abundance constraints are also affected by uncertainties in the physical conditions of the ejecta. In particular, we assume an electron density of $n_e = 10^7(t/9\ \mathrm{days})^{-3}\,\mathrm{cm}^{-3}$, following previous studies (K. Hotokezaka et al. 2023). Lower electron densities result in lower luminosities, which suppress all emission features in the spectra. Higher electron densities, on the other hand, may arise if the ejecta are significantly clumped (J. H. Gillanders et al. 2024). Increasing n_e would strengthen the emission by La III and Ce III, while it would not impact the Te III line, as its emission does not depend on n_e as long as $n_{cr} < n_e$ is satisfied.

The electron temperature and ionization composition adopted in our model are both constrained observationally. The temperature is derived from our blackbody fits, while the ionization state is constrained by the absence of specific emission features (see Sections 3.2 and 3.3). However, the assumption that the electron temperature follows the blackbody temperature may not hold at the late phase. Similarly, our ionization constraints depend on the accuracy of the atomic data, since inaccurately modeled transitions could affect the interpretation of nondetections.

A self-consistent determination of the ejecta properties would require non-LTE calculations that solve for the temperature and ionization evolution of the ejecta while accounting for the contributions of all synthesized elements. Currently, such calculations are limited both by uncertainties in the ejecta's hydrodynamic evolution and by the lack of atomic data required for heavy elements, including recombination coefficients and collision strengths. Therefore, by constraining the model parameters as directly as possible from the observed AT2017gfo spectra, our simple analytic model establishes a benchmark for future studies on the interpretation of kilonova spectra.

5. Summary

We have built an analytic spectral model that computes the luminosity emitted by transitions of heavy elements in an optically thin regime, with the goal of interpreting late-phase kilonova spectra. The model includes selected allowed E1 and forbidden M1 and E2 transitions for all elements with available energy levels in the NIST (A. Kramida et al. 2024) and SCASA (J. Blaise & J.-F. Wyart 1994) atomic databases. By individually computing the luminosity of each transition, our model predicts emission spectra extending to large wavelengths, with distinct features that depend sensitively on the assumed abundance distribution. Our results indicate that mid-infrared observations will be essential for placing robust constraints on the ejecta composition of future kilonovae.

We apply our model to the late-phase spectra of AT2017gfo, associated with the NSM event GW170817, which mainly exhibits three prominent emission features. We identify La III, Ce III, and Te III as the main contributors to the observed 1.4, 1.6, and 2.1 μm features, respectively. Using radiative and collisional rates newly computed with the atomic structure code HULLAC, and R-matrix results of previous works when available, we infer mass fractions of $X(\mathrm{Te}) \approx 0.04$–$0.08$, $X(\mathrm{La}) \approx 0.025$–$0.05$, and $X(\mathrm{Ce}) \approx 0.05$–$0.1$. The constraints on La and Ce remain tentative, however, due to uncertainties in the origin of the radiation field. From the nondetection of Kr and Sb features, we further derive upper limits of $X(\mathrm{Kr}) \lesssim 0.03$

and $X(\mathrm{Sb}) \lesssim 0.003$. These abundance constraints suggest that the nucleosynthesis in the inner ejecta of GW170817 produced a suppressed first *r*-process peak and enhanced production of heavier elements relative to the solar *r*-process abundance pattern. This result is consistent with nucleosynthesis inferred from observations of metal-poor stars enhanced in *r*-process. Furthermore, under the assumption that the relative abundances of heavy *r*-process elements follow the solar pattern, our Te abundance implies a lanthanide fraction of $X_{\mathrm{LN}} \approx (3\text{–}6) \times 10^{-2}$, comparable to values inferred for *r*-enhanced metal-poor stars ($X_{\mathrm{LN}} \approx 3 \times 10^{-2}$; A. P. Ji et al. 2019).

Our work provides robust identifications of all late-phase spectral features observed in AT2017gfo and new abundance constraints derived from those features. Further progress will require improved atomic data for heavy elements and fully self-consistent non-LTE calculations of the ejecta evolution. The results presented here provide a benchmark for such efforts and a framework for interpreting late-time spectra from future kilonova events.

Acknowledgments

We thank the anonymous referee for constructive feedback. S.R. acknowledges support from the Graduate Program on Physics for the Universe (GP-PU) at Tohoku University. This work is supported by the Grant-in-Aid for Scientific Research from JSPS (grant Nos. 23H00127, 23H04894, 23H04891, 23H05432, 26K00732, 26K21726) and the JST FOREST Program (grant No. JPMJFR212Y).

Appendix A
Candidate Elements

We discuss here the viable candidate species for each feature, all summarized in Table A1 with their relevant transitions and reason for exclusion. In this Section, we adopt the atomic data from our HULLAC atomic structure calculations when available (Appendix B) to test for the relevance of selected elements. To avoid confusion, we refer hereafter to our analytic model that uses the original atomic data approximations introduced in Section 2.2 as approximated model, while our model computed with the updated HULLAC atomic data is referred to as the HULLAC model.

A.1. 1.4 μm Feature

Ge I ($Z = 32$): Assuming the solar abundance distribution, we find that [Ge I] 1.4034 μm may explain the 1.4 μm feature. However, with the collision strength and transition probabilities from HULLAC, we find that the approximated model overestimates the luminosity emitted by this element's transition by 2 orders of magnitude. Furthermore, Figure 4 shows that Ge I has other stronger M1 transitions that do not match the observed features. This excludes Ge I as a candidate for the 1.4 μm feature.

I II ($Z = 53$): Singly ionized iodine has one fine-structure M1 transition at 1.4111 μm, which is slightly shifted from the observed peak wavelength. I II atomic data computed with HULLAC is overall consistent with our original approximations, and does not exclude this element as a candidate. We therefore estimate the required iodine fraction necessary to reproduce the observation with the HULLAC model, and we show the result in the upper panel of Figure A1. We find that an unphysical mass fraction of $X(\mathrm{I}^{+}) = 0.5$ is required to explain the observations. The strong Te III line suggests that the fraction of singly ionized second *r*-process elements may be small, which would further increase the required iodine mass fraction. We conclude that [I II] 1.4111 μm is most likely not the main candidate for the 1.4 μm feature.

Table A1
List of all Candidates for Each Feature Discussed in This Work, with the Reason for Their Exclusion

Feature	Abundance	Candidate	λ (μm)	Transition	Type	Reason for Exclusion
1.4 μm	Solar	[Ge I]	1.4034	$4s^24p^2\ (^1D_2) \rightarrow 4s^24p^2\ (^3P_0)$	E2	Too weak + nondetection of other transitions
		[I II][a]	1.4111	$5s^25p^4\ (^3P_1) \rightarrow 5s^25p^4\ (^3P_2)$	M1	Too weak
	Heavy	**La III**	**1.3898**	**4f (^{2}F°$_{5/2}$) → 5d (^{2}D$_{3/2}$)**	**E1**	…
			1.4100	**4f (^{2}F°$_{7/2}$) → 5d (^{2}D$_{5/2}$)**	**E1**	…
		[Dy I]	1.4183	$4f^{10}6s^2\ (^5I_6) \rightarrow 4f^{10}6s^2\ (^5I_8)$	E2	Too weak
		Er I	1.3934	$4f^{11}5d6s^2 \rightarrow 4f^{12}6s^2\ (^3H_6)$	E1	Too weak + nondetection of other transitions
		[Ir I]	1.4071	$5d^86s^1\ (^4F_{7/2}) \rightarrow 5d^76s^2\ (^4F_{9/2})$	M1	Too weak + nondetection of other transitions
1.6 μm	Solar	[Rb IV]	1.5973	$4s^24p^4\ (^3P_1) \rightarrow 4s^24p^4\ (^3P_2)$	M1	Too weak
	Heavy	**Ce III**	**1.5961**	**4f5d (^{3}G°$_3$) → 4f^2 (^{3}H$_4$)**	**E1**	…
			1.5852	**4f5d (^{3}G°$_4$) → 4f^2 (^{3}H$_5$)**	**E1**	…
			1.6133	**4f5d (^{3}G°$_5$) → 4f^2 (^{3}H$_6$)**	**E1**	…
		[Ir I]	1.5813	$5d^76s^2\ (^4F_{7/2}) \rightarrow 5d^76s^2\ (^4F_{9/2})$	M1	Too weak + nondetection of other transitions
2.1 μm	Solar	**[Te III][a]**	**2.1048**	**5s^{2}5p^2 (^{3}P$_1$) → 5s^{2}5p^2 (^{3}P$_0$)**	**M1**	…
		[Te I][a]	2.1049	$5s^25p^4\ (^3P_1) \rightarrow 5s^25p^4\ (^3P_2)$	M1	Different ionization
	Heavy	[Ir II]	2.0885	$5d^76s\ (^5F_4) \rightarrow 5d^76s\ (^5F_5)$	M1	Too weak

Notes. Our best candidates for each feature are shown in bold.
[a] [I II], [Te III], and [Te I] appear as candidates for both the solar *r*-process and the heavy element-enhanced abundance distributions, but we only show them here for solar.

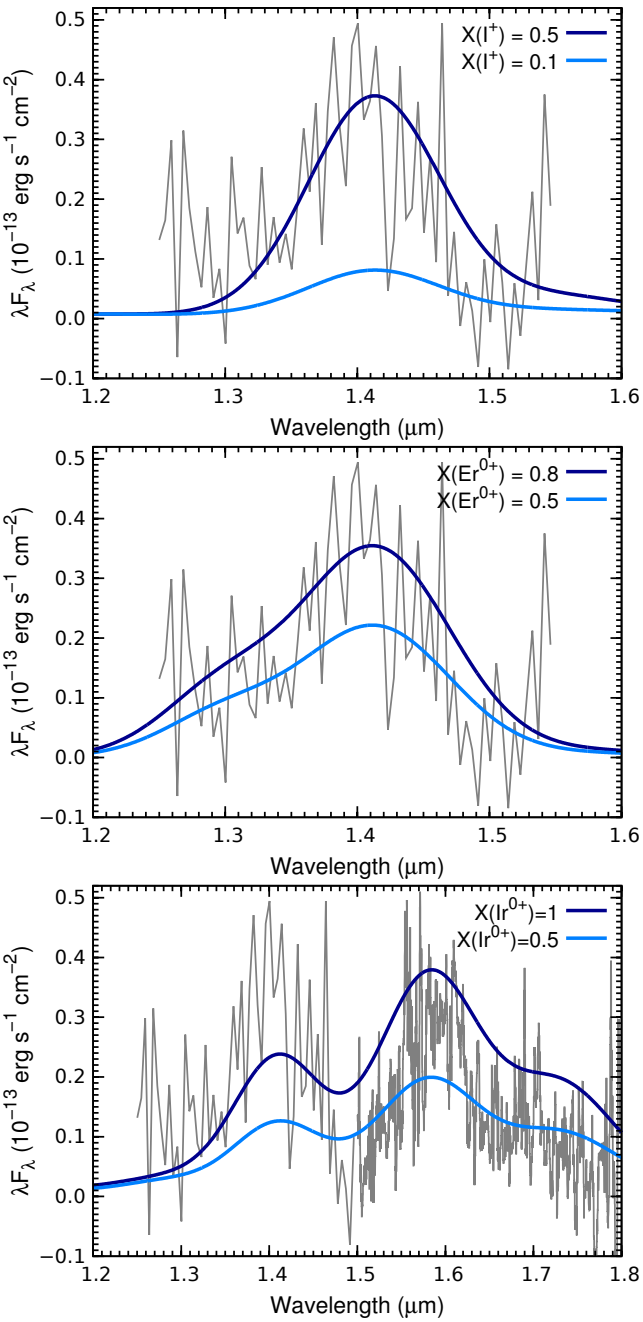


Figure A1. Top: comparison of the synthetic I II feature to the 1.4 μm feature in the HST spectrum at 9.4 days postmerger, assuming different mass fractions of I^+ and a broadening of $v = 0.05\,c$. Middle: same as upper but for Er I feature. Bottom: comparison of the synthetic Ir I features to the 1.4 μm and 1.6 μm features in the HST and VLT spectra at 9.4 days, assuming different mass fractions of Ir^+ and a broadening of $v = 0.05\,c$.

La III ($Z = 57$): This element is our best candidate for the observed 1.4 μm emission feature. It has two strong E1 transitions at 1.3898 and 1.4100 μm, which average matches nicely with the emission line peak wavelength at 1.4 μm. These two lines were also discussed as important candidates for the early-phase absorption feature at $\sim$1.2 μm in AT2017gfo (N. Domoto et al. 2022).

Dy I ($Z = 66$): Dysprosium has one E2 transition at 1.4183 μm. With HULLAC calculations, we find that this transition has an Einstein A-coefficient 6 orders of magnitude lower compared to our original approximations. Therefore, the approximated model largely overestimates the contribution of this transition, and Dy I is excluded as a candidate.

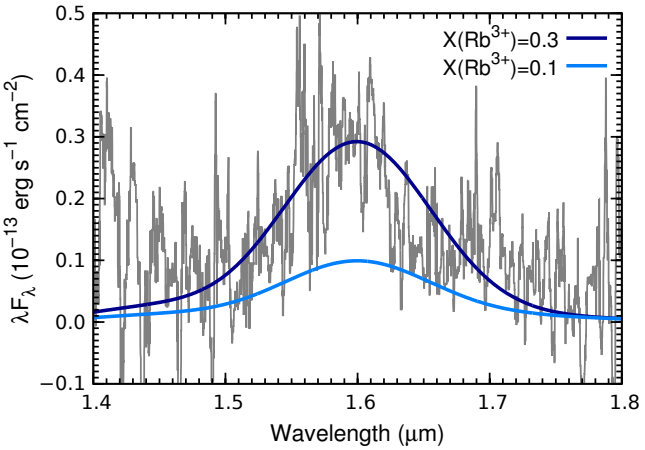


Figure A2. Comparison of the Rb IV feature to the 1.6 μm feature in the VLT spectrum at 9.4 days postmerger, assuming different mass fractions of Rb^{3+} and a line broadening of $v = 0.05\,c$.

Er I ($Z = 68$): This lanthanide element has one E1 transition at 1.3934 μm, matching the observed feature's peak wavelength. In the approximated model, this element's contribution was calculated using the Regemorter formula (Equation (11)) with an Einstein coefficient of $A = 10^6\,s^{-1}$. We could not compute the relevant atomic data of this transition as the upper level's LS-term was not available in the NIST database, which complicates the calibration of theoretical data. However, Er I has another E1 transition and fine-structure M1 transition from the ground level at wavelengths 1.2992 and 1.4371 μm, respectively. A higher fraction of Er I would therefore cause an emission feature that does not match the observations, as shown in the middle panel of Figure A1. Reproducing the observed flux would also require an unphysical mass fraction of $X(Er^{0+}) > 0.5$ with our approximated model. We therefore exclude Er I as a candidate, but we encourage further efforts to compute the necessary atomic data to estimate its importance.

Ir I ($Z = 77$): Iridium has one M1 transition at 1.4071 μm, matching the observations. Due to limitations in HULLAC atomic structure calculations in treating heavy elements, we could not produce better estimates for the collision strengths and radiative transition probabilities for this element. However, since this element has another transition ([Ir I] 1.5812 μm) as a candidate for the 1.6 μm feature (see below), we try either way to model the two features with our approximated model. The bottom panel of Figure A1 shows the comparison of our results to the 9.4 day observations, where we find that an unphysical $X(Ir^{0+}) = 1$ is needed to explain the two features. Furthermore, iridium has other M1 and E2 transitions at 1.7245 and 1.7287 μm, respectively, which do not match the observations as shown in Figure A1. We conclude that Ir I is most likely not the main contributor for both 1.4 and 1.6 μm features, but more accurate atomic data for each of its transitions remain necessary.

A.2. 1.6 μm Feature

Rb IV ($Z = 37$): Assuming the solar abundance distribution, [Rb IV] 1.5973 μm may be considered a candidate for the 1.6 μm feature. Figure A2 shows the results of our HULLAC model for the 1.6 μm feature with the Rb IV transition, where we find that a high mass fraction of $X(Rb^{3+}) = 0.3$ is necessary

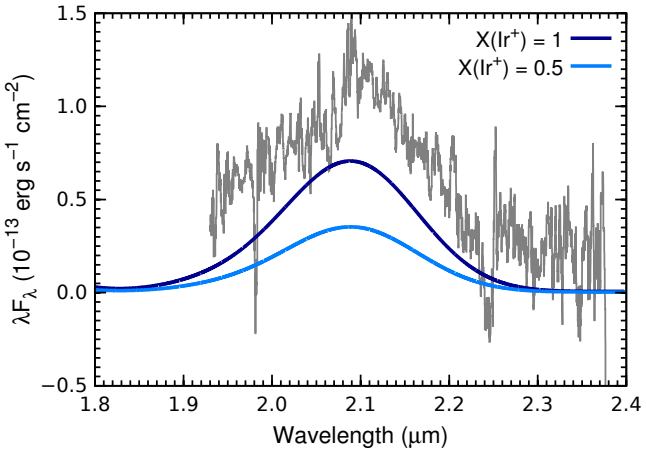


Figure A3. Comparison of the Ir II feature to the 2.1 μm feature in the VLT spectrum at 9.4 days postmerger, assuming different mass fractions of Ir^+ and a line broadening of $v = 0.07\,c$.

to explain the observations. Considering our upper limits on the first *r*-process peak from the nondetection of Kr ($Z = 36$), and the fact that we find no convincing candidate for the 1.4 μm feature assuming the solar abundance distribution pattern, we conclude that Rb is most likely not the main candidate for the feature.

Ce III ($Z = 58$): This is our strongest candidate for the feature at 1.6 μm since it has multiple strong emission lines in the wavelength range of interest. It has three E1 lines at 1.5961, 1.5851, and 1.6133 μm which, on average, match the emission line peak wavelength. These three lines were discussed previously as important candidates for the absorption feature at $\sim$1.5 μm in the early phase (N. Domoto et al. 2022).

Ir I ($Z = 77$): Iridium has one fine-structure line at 1.5812 μm, slightly blueshifted compared to the observed feature's peak. Although we could not provide more accurate atomic data for this element, we find that it is unlikely to be the main candidate for the observed features (see above and Figure A1).

A.3. 2.1 μm Feature

Te III ($Z = 52$): This element has a significantly strong M1 transition at 2.1048 μm, and is our best candidate for the observed feature. It has been previously discussed as the main contributor to the 2.1 μm feature (K. Hotokezaka et al. 2023).

Te I ($Z = 52$): Neutral tellurium also has a strong M1 transition at 2.1049 μm, a similar wavelength to that of the Te III line. As we do not solve for ionization, we cannot draw firm conclusions on which of the two lines is dominant. Previous works solving for non-LTE ionization structure find that the fraction of Te^{0+} is less than 0.1 at around 10 days postmerger (Q. Pognan et al. 2022a; A. Jerkstrand et al. 2026), meaning that the contribution of the Te I line toward this feature may be ignored. We note, however, that the abundance inferred in our analysis for Te would remain roughly consistent even if this feature entirely originated from Te I, since both Te III and Te I lines have a similar wavelength and comparable collision strengths and transition probabilities (Table B2).

Ir II ($Z = 77$): Singly ionized Iridium has a fine-structure transition at 2.0885 μm. This element appears as a candidate for several observed features due to its high abundance as an element belonging to the third *r*-process peak. By assuming that the emission feature is entirely due to Ir II, our approximated model predicts that the required mass fraction is $X(\mathrm{Ir}^+) > 1$ as shown in Figure A3. Such predictions are unphysical, excluding Ir II as a candidate.

Appendix B
HULLAC Calculations

We summarize here the atomic data used in our abundance estimates, computed with the atomic structure code HULLAC (A. Bar-Shalom et al. 2001). HULLAC is an integrated code for calculating the energy levels, cross sections, and radiative transition probabilities of atoms. Orbital functions are derived by solving the single-electron Dirac equation with a central-field potential that includes both a nuclear field and a spherically averaged potential due to electron–electron interactions. Using these orbital functions, *N*-electron configuration state functions are then built as antisymmetric combinations of the orbitals. Relativistic configuration interaction (RCI) calculations are carried out based on these configuration state functions, where the accuracy of the RCI calculations is improved by increasing the number of configurations. This in turn increases the computational cost, especially for complex elements such as lanthanides. In this study, the number of configurations is chosen so that a good balance between accuracy and computational time can be achieved. The accuracy is further improved by optimizing the effective potential following D. Kato et al. (2024). The elements for which we perform HULLAC calculations, as well as the configurations used for the RCI calculations for each atom, are summarized in Table B1. We note here that HULLAC cannot achieve good accuracy for the heaviest elements with $Z \gtrsim 72$ due to their complex atomic structure. Therefore, we choose not to include such calculations in this study.

The transition probabilities and cross sections are calculated with HULLAC for the relevant elements. The energy levels in our analysis are taken from the NIST database and are identified by the *LS*-coupling scheme, while the calculations with HULLAC are performed in the *jj*-coupling scheme. We therefore use the JJ2LSJ extension of the HULLAC code recently developed by G. Gaigalas et al. (2026) to transform HULLAC results into the *LS*-coupling scheme. The energy levels of each transition of interest are then matched to their corresponding energy levels in HULLAC, and the computed transition probabilities are corrected for the change in the transition energy after calibration, such that

$$A_{\mathrm{E1}} = \left(\frac{\lambda}{\lambda_{\mathrm{HULLAC}}}\right)^2 A_{\mathrm{E1;HULLAC}}\,,$$
$$A_{\mathrm{M1}} = \left(\frac{\lambda}{\lambda_{\mathrm{HULLAC}}}\right)^3 A_{\mathrm{M1;HULLAC}}$$
$$A_{\mathrm{E2}} = \left(\frac{\lambda}{\lambda_{\mathrm{HULLAC}}}\right)^5 A_{\mathrm{E2;HULLAC}}\,, \qquad \text{(B1)}$$

Table B1
Configurations Used to Compute the Atomic Data for Featured Species

Ion	$N_{\rm level}$[a]	Configurations
Ge I	156	$4s^24p^2$, $4s^24p^15s^1$, $4s^24p^15p^1$, $4s^24p^14d^1$, $4s^24p^16s^1$, $4s^24p^16p^1$, $4s^24p^15d^1$, $4s^24p^14f^1$, $4s^24p^17s^1$, $4s^24p^17p^1$, $4s^24p^18s^1$, $4s^24p^16d^1$, $4p^4$, $4s^14p^25s^1$, $4s^14d^25s^1$, $4s^14p^15s^2$
Kr II	354	$4s^24p^5$, $4s^14p^6$, $4s^24p^45s^1$, $4s^24p^44d^1$, $4s^24p^45p^1$, $4s^24p^45d^1$, $4s^24p^46s^1$, $4s^24p^46p^1$, $4s^24p^44f^1$, $4s^24p^47s^1$, $4s^24p^46d^1$, $4s^24p^45f^1$, $4s^24p^48s^1$, $4s^24p^46f^1$, $4s^24p^47f^1$, $4s^24p^48f^1$, $4s^24p^35s^2$, $4s^14p^55s^1$, $4s^14p^54d^1$, $4s^14p^45s^2$
Kr III	1669	$4s^24p^4$, $4s^14p^5$, $4s^24p^34d^1$, $4s^24p^35s^1$, $4s^24p^35p^1$, $4s^24p^36s^1$, $4s^24p^36d^1$, $4p^6$, $4s^24p^14d^3$, $4s^24d^4$, $4s^14p^34d^2$, $4s^14p^24d^3$, $4s^14p^14d^4$, $4p^44d^2$, $4s^24p^24d^2$, $4s^24p^25s^2$
Rb IV	406	$4s^24p^4$, $4s^14p^5$, $4s^24p^34d^1$, $4s^24p^35s^1$, $4s^24p^35p^1$, $4s^24p^35d^1$, $4s^24p^36s^1$
Sn II	61	$5s^25p^1$, $5s^15p^2$, $5s^26s^1$, $5s^25d^1$, $5s^26p^1$, $5s^27s^1$, $5s^24f^1$, $5s^26d^1$, $5s^27p^1$, $5s^28s^1$, $5s^25f^1$, $5s^27d^1$, $5s^28p^1$, $5s^29p^1$, $5s^15p^16s^1$, $5s^15p^15d^1$
Sb III	88	$5s^25p^1$, $5s^15p^2$, $5s^26s^1$, $5s^25d^1$, $5s^26p^1$, $5s^27s^1$, $5s^26d^1$, $5s^24f^1$, $5s^28s^1$, $5p^3$, $5s^15p^16s^1$, $5s^15p^15d^1$, $5s^15p^17s^1$, $5s^16s^2$, $5s^16d^2$, $5p^26s^1$
Te I	602	$5p^4$, $5p^36s^1$, $5p^26s^2$, $5p^36p^1$, $5p^35d^1$, $5p^37s^1$, $5p^37p^1$, $5p^36d^1$, $5p^38s^1$, $5p^38p^1$, $5p^35f^1$, $5p^25d^2$, $5p^15d^3$, $5p^26s^16p^1$, $5p^16s^26p^1$, $5p^26s^15d^1$, $5p^26s^17s^1$, $5p^16s^25d^1$, $6s^26p^2$
Te III	273	$5s^25p^2$, $5s^15p^3$, $5s^25p^15d^1$, $5s^25p^16s^1$, $5s^25p^17s^1$, $5s^25p^16d^1$, $5s^25p^14f^1$, $5s^25p^16p^1$, $5p^4$, $5s^15p^25d^1$, $5s^15p^26s^1$, $5s^15p^16s^2$, $5s^15p^27s^1$, $5s^25d^2$, $5d^4$, $5s^26s^2$, $5s^15p^25d^1$, $5p^35d^1$, $5p^36s^1$, $5p^37s^1$, $5p^26s^2$
I II	406	$5s^25p^4$, $5s^25p^36s^1$, $5s^15p^5$, $5s^25p^35d^1$, $5s^25p^36p^1$, $5s^25p^37s^1$, $5s^25p^36d^1$, $5s^25p^34f^1$, $5s^25p^37p^1$, $5s^25p^38s^1$, $5s^25p^36d^1$, $5s^25p^37d^1$, $5s^25p^35f^1$, $5s^25p^38s^1$, $5p^6$, $5s^25p^26s^2$, $5s^25p^25d^2$
La III	137	$5p^65d^1$, $5p^64f^1$, $5p^66s^1$, $5p^66p^1$, $5p^67p^1$, $5p^66p^1$, $5p^67s^1$, $5p^66d^1$, $5p^65f^1$, $5p^68s^1$, $5p^67d^1$, $5p^65g^1$, $5p^66f^1$, $5p^68p^1$, $5p^69s^1$, $5p^68d^1$, $5p^55d^2$, $5p^55d^16s^1$, $5p^56s^2$, $5p^56s^16p^1$, $5p^55d^17s^1$
Ce III	230	$4f^2$, $4f^15d^1$, $4f^16s^1$, $5d^2$, $4f^16p^1$, $5d^16s^1$, $4f^16d^1$, $4f^17s^1$, $5d^16p^1$, $4f^15f^1$ $4f^17p^1$, $4f^18s^1$, $4f^16f^1$, $4f^15g^1$, $6p^2$, $5d^16d^1$, $6s^2$, $6s^16p^1$, $5d^17s^1$, $6s^16d^1$
Dy I	5161	$4f^{10}6s^2$, $4f^95d^16s^2$, $4f^{10}6s^16p^1$, $4f^{10}5d^16s^1$

Note.
[a] Number of levels computed with HULLAC for each ion.

where $A_{\rm E1}$, $A_{\rm M1}$, and $A_{\rm E2}$ are the Einstein A-coefficients for electric dipole, magnetic dipole, and electric quadrupole transitions, respectively. The transition energies ΔE calculated with HULLAC and the corresponding values from NIST (A. Kramida et al. 2024), along with the corrected transition probabilities of key transitions, are summarized in Table B2. Larger discrepancies between HULLAC and NIST transition energies appear mainly for transitions between different electron configurations, while relatively good agreement is obtained for forbidden fine-structure transitions within the same configuration. These discrepancies may reflect possible uncertainties in the relative energies of the configurations in the atomic structure calculations; however, they do not directly imply comparable uncertainties in the computed collision strengths.

For transitions that are allowed in both magnetic dipole and electric quadrupole radiation, both $A_{\rm M1}$ and $A_{\rm E2}$ are calculated, and the total transition probability in our model is taken as

$$g\bar{A} = gA_{\rm M1} + gA_{\rm E2}. \tag{B2}$$

Table B2 also shows the energy-averaged collision strength of the key elements. The collisional cross sections are computed with HULLAC for a sample of input projectile energies, from which we compute the energy-specific collision strength for each input energy, based on the relation

$$\sigma_{12}(v) = \frac{\pi\hbar^2}{m_{\rm e}^2 v^2}\frac{\Omega_{12}}{g_1}. \tag{B3}$$

The energy-averaged collisional strength is then computed using Equation (3) assuming $T = 2000$ K.

Table B2
Radiative Transition Probabilities and Energy-averaged Collision Strengths Calculated with HULLAC for Featured Species

Ion	λ (μm)	ΔE[a] (eV)		gA_{E1} (s^{-1})	gA_{M1} (s^{-1})	gA_{E2} (s^{-1})	Υ[b]
		NIST	HULLAC				
Ge I	1.4034	0.883	0.746	⋯	⋯	3.42×10^{-4}	0.23
Kr II	1.8622	0.666	0.845	⋯	23.8	0.18	1.24
Kr III	2.1986	0.564	0.621	⋯	11.1	9.65×10^{-3}	0.56
	1.8822	0.659	0.701	⋯	⋯	7.67×10^{-3}	0.79
Rb IV	1.5973	0.776	0.871	⋯	32.2	3.92×10^{-2}	0.54
Sn II	2.3521	0.527	0.554	⋯	3.79	2.66×10^{-2}	3.44
Sb III	1.5207	0.815	0.793	⋯	8.83	4.81×10^{-2}	2.16
Te I	2.1049	0.589	0.566	⋯	5.52	1.42×10^{-2}	1.57
Te III	2.1048	0.589	0.579	⋯	4.98	⋯	1.65
I II	1.4111	0.879	0.885	⋯	23.7	7.93×10^{-2}	1.16
La III	1.3898	0.892	2.78	6.20×10^{8}	⋯	⋯	3.02
	1.4100	0.879	2.75	9.41×10^{8}	⋯	⋯	3.11
Ce III	1.5852	0.782	1.26	4.81×10^{7}	⋯	⋯	4.40
	1.5961	0.777	1.21	3.32×10^{7}	⋯	⋯	4.39
	1.6133	0.769	1.28	6.80×10^{7}	⋯	⋯	4.69
	1.9146	0.648	0.718	1.29×10^{6}	⋯	⋯	1.34
	1.9504	0.636	0.651	2.96×10^{5}	⋯	⋯	0.75
	1.9976	0.621	0.944	⋯	1.14	2.07×10^{-7}	7.15×10^{-2}
	2.0691	0.599	0.638	6.75×10^{5}	⋯	⋯	1.24
	2.0987	0.591	0.717	⋯	2.21×10^{-2}	9.34×10^{-4}	0.39
Dy I	1.4183	0.874	0.814	⋯	⋯	$9{,}38 \times 10^{-8}$	0.41

Note.
[a] Transition energy from the NIST ADS and the computed transition energy with HULLAC.
[b] Energy-averaged collision strength (Equation (3) with $T = 2000$ K).

ORCID iDs

Salma Rahmouni https://orcid.org/0009-0002-1232-243X
Masaomi Tanaka https://orcid.org/0000-0001-8253-6850
Daiji Kato https://orcid.org/0000-0002-5302-073X
Gediminas Gaigalas https://orcid.org/0000-0003-0039-1163
Kenta Hotokezaka https://orcid.org/0000-0002-2502-3730

References

Abac, A. G., Abouelfettouh, I., Acernese, F., et al. 2026, ApJL, 1005, L51
Abbott, B. P., Abbott, R., Abbott, T. D., et al. 2017a, PhRvL, 119, 161101
Abbott, B. P., Abbott, R., Abbott, T. D., et al. 2017b, ApJL, 848, L12
Arcavi, I., Hosseinzadeh, G., Howell, D. A., et al. 2017, Natur, 551, 64
Arya, A., Damgaard, R., Sneppen, A., et al. 2026, arXiv:2604.05812
Bahcall, J. N., & Wolf, R. A. 1968, ApJ, 152, 701
Banerjee, S., Jerkstrand, A., Badnell, N., et al. 2025, ApJ, 992, 19
Bar-Shalom, A., Klapisch, M., & Oreg, J. 2001, JQSRT, 71, 169
Blaise, J., & Wyart, J.-F. 1994, SCASA Database, http://www.lac.universite-paris-saclay.fr/Data/Database
Bromley, S., Garbe, E., McElroy, N., et al. 2026, arXiv:2603.00346
Chiba, K., Tanaka, M., Wanajo, S., et al. 2026, arXiv:2604.05703
Chornock, R., Berger, E., Kasen, D., et al. 2017, ApJL, 848, L19
Ding, M., Ryabtsev, A., Kononov, E., et al. 2024, A&A, 684, A149
Domoto, N., Hotokezaka, K., & Kasen, D. 2026, arXiv:2607.00433
Domoto, N., Tanaka, M., Kato, D., et al. 2022, ApJ, 939, 8
Domoto, N., Tanaka, M., Wanajo, S., & Kawaguchi, K. 2021, ApJ, 913, 26
Domoto, N., Wanajo, S., Tanaka, M., Kato, D., & Hotokezaka, K. 2025, ApJ, 978, 99
Domoto, N., Lee, J.-J., Tanaka, M., et al. 2023, ApJ, 956, 113
Dougan, D. J., McElroy, N. E., Ballance, C. P., & Ramsbottom, C. A. 2025, MNRAS, 541, 367
Eichler, D., Livio, M., Piran, T., & Schramm, D. N. 1989, Natur, 340, 126
Fishbach, M., Ji, A. P., Fong, W.-f., et al. 2026, ApJL, 1006, L49
Flörs, A., Ferreira da Silva, R., Marques, J. P., Sampaio, J. M., & Martínez-Pinedo, G. 2026, PhRvD, 113, 063041
Freiburghaus, C., Rosswog, S., & Thielemann, F.-K. 1999, ApJL, 525, L121
Fujibayashi, S., Kiuchi, K., Wanajo, S., et al. 2023, ApJ, 942, 39
Gaigalas, G., Kato, D., & Tanaka, M. 2026, JQSRT, 363, 110058
Ghirlanda, G., Salafia, O. S., Paragi, Z., et al. 2019, Sci, 363, 968
Gillanders, J. H., Flors, A., & Ferreira da Silva, R. 2026, MNRAS, 548, stag748
Gillanders, J. H., Sim, S. A., Smartt, S. J., Goriely, S., & Bauswein, A. 2024, MNRAS, 529, 2918
Gillanders, J. H., & Smartt, S. J. 2025, 538, 1663
Gillanders, J. H., Smartt, S. J., Sim, S. A., Bauswein, A., & Goriely, S. 2022, MNRAS, 515, 631
Gillanders, J. H., Troja, E., Fryer, C. L., et al. 2023, arXiv:2308.00633
Goriely, S., Bauswein, A., & Janka, H.-T. 2011, ApJL, 738, L32
Hotokezaka, K., Beniamini, P., & Piran, T. 2018, IJMPD, 27, 1842005
Hotokezaka, K., & Nakar, E. 2020, ApJ, 891, 152
Hotokezaka, K., Tanaka, M., Kato, D., & Gaigalas, G. 2021, MNRAS, 506, 5863
Hotokezaka, K., Tanaka, M., Kato, D., & Gaigalas, G. 2022, MNRAS, 515, L89
Hotokezaka, K., Tanaka, M., Kato, D., & Gaigalas, G. 2023, MNRAS, 526, L155
Jerkstrand, A., Pognan, Q., Banerjee, S., et al. 2026, MNRAS, 548, stag733
Ji, A. P., Drout, M. R., & Hansen, T. T. 2019, ApJ, 882, 40
Kasen, D., Metzger, B., Barnes, J., Quataert, E., & Ramirez-Ruiz, E. 2017, Natur, 551, 80
Kato, D., Tanaka, M., Gaigalas, G., Kitovienė, L., & Rynkun, P. 2024, MNRAS, 535, 2670
Kawaguchi, K., Shibata, M., & Tanaka, M. 2018, ApJL, 865, L21
Kilpatrick, C. D., Foley, R. J., Kasen, D., et al. 2017, Sci, 358, 1583
Kitamura, A., Kawaguchi, K., Tanaka, M., & Fujibayashi, S. 2025, ApJ, 982, 97
Kramida, A., Ralchenko, Y., Reader, J. & NIST ASD Team 2024, NIST Atomic Spectra Database, v5.12,
Kupka, F., Piskunov, N., Ryabchikova, T. A., Stempels, H. C., & Weiss, W. W. 1999, A&AS, 138, 119
Lattimer, J. M., & Schramm, D. N. 1974, ApJL, 192, L145
Levan, A. J., Gompertz, B. P., Salafia, O. S., et al. 2024, Natur, 626, 737
Li, L.-X., & Paczyński, B. 1998, ApJL, 507, L59
Metzger, B. D., Martínez-Pinedo, G., Darbha, S., et al. 2010, MNRAS, 406, 2650

McMillan, P. J. 2011, MNRAS, 414, 2446
Mooley, K. P., Frail, D. A., Dobie, D., et al. 2018, ApJL, 868, L11
Mulholland, L. P., Bromley, S. J., Ballance, C. P., Sim, S. A., & Ramsbottom, C. A. 2025, JQSRT, 345, 109545
Mulholland, L. P., Ferguson, N., Shingles, L. J., et al. 2026a, arXiv:2609.15900
Mulholland, L. P., McElroy, N. E., McNeill, F. L., et al. 2024a, MNRAS, 532, 2289
Mulholland, L. P., McNeill, F., Sim, S. A., Ballance, C. P., & Ramsbottom, C. A. 2024b, MNRAS, 534, 3423
Mulholland, L. P., Ramsbottom, C. A., Ballance, C. P., Sneppen, A., & Sim, S. A. 2026b, MNRAS, 546, stag237
Pasternack, S. 1940, ApJ, 92, 129
Perego, A., Bernuzzi, S., & Radice, D. 2019, EPJA, 55, 124
Perego, A., Vescovi, D., Fiore, A., et al. 2022, ApJ, 925, 22
Pian, E., D'Avanzo, P., Benetti, S., et al. 2017, Natur, 551, 67
Piskunov, N. E., Kupka, F., Ryabchikova, T. A., Weiss, W. W., & Jeffery, C. S. 1995, A&AS, 112, 525
Pognan, Q., Grumer, J., Jerkstrand, A., & Wanajo, S. 2023, MNRAS, 526, 5220
Pognan, Q., Jerkstrand, A., & Grumer, J. 2022a, MNRAS, 510, 3806
Pognan, Q., Jerkstrand, A., & Grumer, J. 2022b, MNRAS, 513, 5174
Pognan, Q., Kawaguchi, K., Wanajo, S., Fujibayashi, S., & Jerkstrand, A. 2026, MNRAS, 547, stag441
Prantzos, N., Abia, C., Cristallo, S., Limongi, M., & Chieffi, A. 2020, MNRAS, 491, 1832
Rahmouni, S., Tanaka, M., Domoto, N., et al. 2025, ApJ, 980, 43
Ricigliano, G., Hotokezaka, K., & Arcones, A. 2025, MNRAS, 543, 2534
Roberts, L. F., Kasen, D., Lee, W. H., & Ramirez-Ruiz, E. 2011, ApJL, 736, L21
Roederer, I. U., Sakari, C. M., Placco, V. M., et al. 2018, ApJ, 865, 129
Roederer, I. U., Lawler, J. E., Den Hartog, E. A., et al. 2022, ApJS, 260, 27
Rosswog, S., Sollerman, J., Feindt, U., et al. 2018, A&A, 615, A132
Ryabchikova, T., Piskunov, N., Kurucz, R. L., et al. 2015, PhyS, 90, 054005
Schoning, T. 1997, A&AS, 122, 277
Shibata, M., Fujibayashi, S., Hotokezaka, K., et al. 2017, PhRvD, 96, 123012
Shortley, G. H. 1940, PhRv, 57, 225
Smartt, S. J., Chen, T.-W., Jerkstrand, A., et al. 2017, Natur, 551, 75
Sneden, C., Cowan, J. J., Lawler, J. E., et al. 2003, ApJ, 591, 936
Sneppen, A., Damgaard, R., Watson, D., et al. 2024, A&A, 692, A134
Sneppen, A., & Watson, D. 2023, A&A, 675, A194
Symbalisty, E., & Schramm, D. N. 1982, ApL, 22, 143
Tanaka, M., Utsumi, Y., Mazzali, P. A., et al. 2017, PASJ, 69, 102
Tanaka, M., Domoto, N., Aoki, W., et al. 2023, ApJ, 953, 17
Tanvir, N. R., Levan, A. J., González-Fernández, C., et al. 2017, ApJL, 848, L27
Tarumi, Y., Hotokezaka, K., Domoto, N., & Tanaka, M. 2023, arXiv:2302.13061
Utsumi, Y., Tanaka, M., Tominaga, N., et al. 2017, PASJ, 69, 101
van Regemorter, H. 1962, ApJ, 136, 906
Wanajo, S., Sekiguchi, Y., Nishimura, N., et al. 2014, ApJL, 789, L39
Watson, D., Hansen, C. J., Selsing, J., et al. 2019, Natur, 574, 497